Technical Document 2566
May 1994

Convergence and Error Estimation in the Method of Moments

T. O. Jones, III

Naval Command, Control and
Ocean Surveillance Center
RDT&E Division

San Diego, CA
92152-5001

DISCLAIMER NOTICE
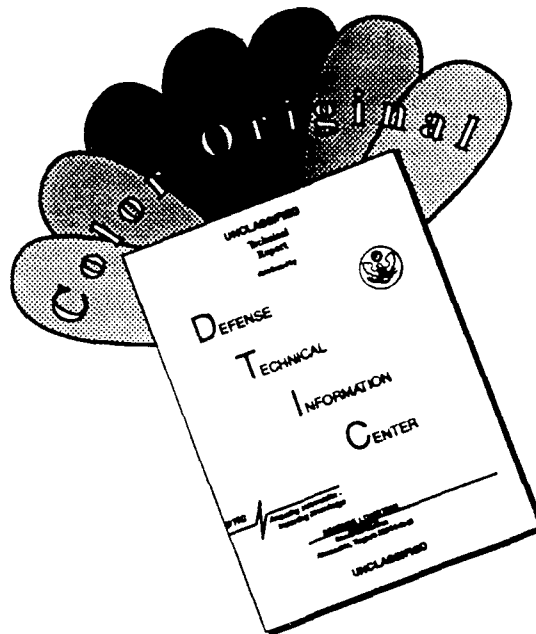
THIS DOCUMENT IS BEST
QUALITY AVAILABLE. THE COPY
FURNISHED TO DTIC CONTAINED
A SIGNIFICANT NUMBER OF
COLOR PAGES WHICH DO NOT
REPRODUCE LEGIBLY ON BLACK
AND WHITE MICROFICHE.

Technical Document 2566
March 1996

Convergence and Error Estimation in the Method of Moments

T. O. Jones, III

NAVAL COMMAND, CONTROL AND OCEAN SURVEILLANCE CENTER RDT&E DIVISION
San Diego, California 92152-5001

K. E. EVANS, CAPT, USN
Commanding Officer

R. T. SHEARER
Executive Director

ADMINISTRATIVE INFORMATION

Released by
A. G. Crane, Jr., Head
Systems Development Branch

Under authority of
D. M. Bauman, Head
Submarine Communications
& C⁴I Systems Division

SB

NAVAL COMMAND, CONTROL AND OCEAN SURVEILLANCE CENTER
RESEARCH, DEVELOPMENT, TEST & EVALUATION DIVISION
SAN DIEGO, CALIFORNIA 92152-5001

6 February 1997

Technical Document 2566
Convergence and Error Estimation in the Method of Moments
By: T.O. Jones, III
Dated: March 1996

Literature Change

1. Replace the existing cover, title page, and Administrative Information page with the attached corrected pages.

2. Replace the existing Form 298 with the attached corrected pages.

3. Replace the existing Initial Distribution list with the attached corrected page.

CONTENTS

Figures

Tables

AD-A317065

REPORT DOCUMENTATION PAGE

Form Approved
OMB No. 0704-0188

1. AGENCY USE ONLY *(Leave blank)*	2. REPORT DATE	3. REPORT TYPE AND DATES COVERED
	May 1994	Final: October 1990 – September 1993

4. TITLE AND SUBTITLE

CONVERGENCE AND ERROR ESTIMATION IN THE METHOD OF MOMENTS

5. FUNDING NUMBERS

PE: 0601152N
AN: DN300163
WU: 83–ZW52

6. AUTHOR(S)

T. O. Jones, III

7. PERFORMING ORGANIZATION NAME(S) AND ADDRESS(ES)

Office of Naval Research
800 N. Quincy Street
Arlington, VA 22217–5000

8. PERFORMING ORGANIZATION REPORT NUMBER

TD 2566

9. SPONSORING/MONITORING AGENCY NAME(S) AND ADDRESS(ES)

Naval Command, Control and Ocean Surveillance Center (NCCOSC)
RDT&E Division
San Diego, California 92152–5000

10. SPONSORING/MONITORING AGENCY REPORT NUMBER

11. SUPPLEMENTARY NOTES

12a. DISTRIBUTION/AVAILABILITY STATEMENT

Approved for public release; distribution is unlimited.

12b. DISTRIBUTION CODE

13. ABSTRACT *(Maximum 200 words)*

In this report, we developed a new algorithm for modeling thin wire antennas. The basis functions, boundary condition, and impedance matric are formulated to minimize the impact of errors on the accuracy of the charge distribution. The charge distribution on a segment is modeled with multipole basis functions. The high-order multipoles basis functions interact primarily with the charge distribution on neighboring segments. The boundary condition limits the error in the charge distribution to high-order multipoles. Consequently, the errors introduced by the boundary condition are local. The boundary condition also allows the errors on each segment to be estimated. The error in the boundary condition is the product of the boundary condition error matrix and the solution. The boundary condition error matrix and the impedance matrix arde computed at the same time. The stability and convergence of the algorithm is illustrated by computing the input impedance and the charge distribution of the symmetric dipole. The concepts used to define the basis functions and boundary conditions can be applied to general antenna problems. However, the computer code is limited to the modeling of the symmetric dipole.

14. SUBJECT TERMS

Mission Area: Communications

thin-wire antennas	multipole fields
multipole basis functions	near field
boundary condition	intermediate field
method of moments	far field
Legendre Polynomials	

15. NUMBER OF PAGES

109

16. PRICE CODE

17. SECURITY CLASSIFICATION OF REPORT	18. SECURITY CLASSIFICATION OF THIS PAGE	19. SECURITY CLASSIFICATION OF ABSTRACT	20. LIMITATION OF ABSTRACT
UNCLASSIFIED	UNCLASSIFIED	UNCLASSIFIED	SAME AS REPORT

21a. NAME OF RESPONSIBLE INDIVIDUAL	21b. TELEPHONE *(include Area Code)*	21c. OFFICE SYMBOL
T. O. Jones, III	(619) 553-7082 tojones@nosc.mil	Code D835

1 INTRODUCTION

In numerical antenna modeling, the charge and current distribution can have convergence problems. The charge and current distribution may not converge as the number of basis functions in the model are increased. Dudley (1985) discusses mathematical and numerical problems in the method-of-moments solution of antenna problems. The electromagnetic method-of-moments approach has mathematical limitations that contribute to the convergence problems. These mathematical problems are not present in the electrostatic method-of-moments approach. Insight into the limitations of the method-of-moments approach can be gained by considering electrically small antennas. The algorithm developed in this report improves the convergence of the method-of-moments approach. This algorithm allows the error in the boundary condition to be estimated on each segment.

The numerical limitations of the method of moments can be understood by considering electrically small antennas. Electrically small antennas can be analyzed with the quasi-static approach or with the full-wave approach. In principle, the full-wave approach should have the same accuracy and stability properties as the quasi-static approach. The only difference in the two methods is the numerical formulation of the problem.

In the quasi-static approach, the interaction between the charges is divided into two parts: the static and frequency-dependent interaction terms. The static interaction terms are much larger than the frequency-dependent interaction terms. The static interaction term is used to compute the static-charge distribution. The current and frequency-dependent part of the interaction give a small correction to the static-charge distribution. The quasi-static approach is numerically very stable and accurate; however, it is limited to electrically small antennas.

In the full-wave method-of-moments approach, the static and frequency-dependent interaction terms are combined in one matrix, the impedance matrix. For electrically

1

small antennas, the frequency-dependent terms cancel out in the solution of the impedance matrix. The cancellation of the frequency-dependent terms leads to round-off errors in the solution of the matrix. The full-wave method-of-moments approach is not as stable or accurate as the quasi-static approach.

The basis functions and boundary condition developed in this report simplify the structure of the impedance matrix. For electrically small antennas, the impedance matrix has large static interaction terms with small frequency-correction terms. The quasi-static properties of electrically small antennas are explicit in the structure of the impedance matrix. This improves the stability and accuracy of the full-wave approach without limiting the scope of the applications. *This approach provides a better understanding of the error in the method of moments.*

The idea for the numerical algorithm described in this report developed out of an effort to improve the convergence of MININEC 3. The MININEC 3 code, developed by Logan and Rockway (1986), uses square pulses to model antenna-current distributions. The square-pulse charge distributions are implicit to the MININEC 3 code. This simple model gives surprisingly good results. The problem with a square-pulse charge distribution is that it does not eliminate the parallel component of the electric field on individual segments of the wire. In nature, the charges would redistribute themselves to eliminate the parallel component of the electric fields.

The charge and current basis functions discussed in this report emulate nature. The net charge on a segment is modeled by a square pulse. The higher order basis functions are used to redistribute the charge on each segment to eliminate the electric field along the segments. Legendre polynomials[1] (Richmond, 1965) are used for the charge basis functions. The above observations were the motivation for the numerical model developed in

---

1. J. H. Richmond expanded a current distribution, computed with sine and cosine basis functions, with Chebyshev and Legendre polynomial series, which give faster convergence.

this report. The general antenna problem is too complex for an initial numerical electro-magnetic code. A numerical code for the symmetric dipole is used to test this approach to numerical electromagnetic modeling.

In section 2, the stability and convergence of this algorithm are illustrated with a computer model of a dipole. The admittance at resonance and antiresonance of the dipole is computed using one to seven basis functions per segment. The admittance for the one, two, and seven basis function models are plotted against the matrix size. The admittance curves agree with King's (1956) calculations for the resonance and antiresonance of the dipole. *Their convergence and accuracy are a consequence of the new boundary condition.*

For electrically small antennas, the charge distribution can be compared to the static charge distribution (Watt, 1967). A 24×24 and a 48×48 impedance matrix were used to show the convergence of the charge distribution model. Different combinations of seg-ments and basis functions were used to model the charge distribution. A simple model with two basis functions per segment gives an accurate model of the static charge distribu-tion on the interior segments in the model. A model with eight basis functions per segment gives the best results for the charge distribution on the entire antenna. The accuracy of the model at the end of the wire is improved by use of a 84×84 impedance matrix with 12 segments and seven basis functions per segment. These results show that the charge distribution converges as the number of basis functions is increased. The numerical results indicate a very stable model of the thin-wire dipole.

The development of the algorithm includes a discussion of the different types of errors in the algorithm. The errors fall into two classes: modeling and computational errors. The basis functions used to model the charge distribution are only an approxima-tion of the correct charge distribution. The second modeling error is caused by the approx-imation of the ideal boundary condition. Error in the boundary condition induces errors in the charge and current distributions. The interaction of the two modeling errors is deter-mined by the numerical algorithm used in computing and imposing the boundary condi-

3

tion. The numerical algorithm includes several sources of computational errors: evaluation of the fields, imposing the boundary condition, and solution of the impedance matrix. The following discussion is a qualitative discussion of the interaction of the different errors in our numerical formulation of the dipole antenna model.

The notation is developed in section 3. This notation allows a detailed discussion of the charge and current distribution on each segment in the antenna. The scalar and vector potentials on each segment are a function of the charge and current basis function on the other segments. The scalar and vector potentials are used to formulate the boundary condition on each segment.

The Legendre-polynomial charge basis functions are discussed in section 4. The current basis functions are computed from the continuity equation and the charge basis functions. The charge distribution is modeled by N basis functions, $P_0(t)$ to $P_{N-1}(t)$, for each segment of the antenna. The charge distribution modeling error is $P_N(t)$, $P_{N+1}(t)$, plus additional higher order basis functions. The modeling error in the charge distribution causes errors in the scalar and vector potentials.

Section 5 shows that the Legendre polynomials are a multipole expansion of the charge distribution on the segment. The potential integral of each basis function contributes to the far, intermediate, and near fields. The potential in each region is discussed in detail. The static part of the potential falls off as $r^{-(n+1)}$ for the nth Legendre polynomial. The modeling error in the charge distribution impacts the potentials and boundary condition only on nearby segments. This algorithm is compared to the matrix transformation technique developed by Canning (1992). The numerical calculation of the scalar and vector potentials is discussed in detail in section 6.

The scalar and vector potentials are computed from the Legendre polynomial potential integral, which is the integral of the surface charge distribution and the free-space Green's function. The integral is evaluated by integrating along the length of the segment first, and then integrating around the circumference. The integration around the circum-

4

ference is evaluated by Gauss-Chebyshev integration, which has a very simple physical interpretation. It is equivalent to replacing the surface charge with equally spaced lines of charge parallel to the axis of the cylinder. This simple physical interpretation of the potential integral is used to deduce the error term for the numerical integration.

A sequence of Gauss-Chebyshev integration formulas can be used to estimate the error in the angular integration. Some examples are used to illustrate the convergence of the numerical evaluation. In addition, the static potential near the end of the segment is plotted to show the sharp drop in the potential at the end of the segment. The potential integral can be computed with arbitrary accuracy. The calculation of the potential integral does not introduce errors into the boundary condition.

In principle, the electric field should be normal to the surface of a perfect conductor at all points on the surface. In the method of moments, the ideal boundary is replaced by an approximation of the boundary condition. The modeling errors introduced by the boundary condition are discussed in section 7. In addition, we discuss numerical errors introduced by the numerical evaluation of the boundary condition. The numerical and modeling errors primarily create high multipole errors in the charge distribution. These errors impact only the nearby segments. The numerical method used to calculate the boundary condition can be used to estimate the error in the boundary condition.

In section 8, we derive the impedance matrix created by these basis functions and the boundary conditions. The impedance matrix neglects some high multipole moment terms introduced by the current basis functions. The errors caused by this approximation are local to each segment. The local error on each segment can be computed by extending the impedance matrix to include extra boundary condition expansion coefficients. These extra boundary condition expansion coefficients represent the error in the boundary condition on each segment.

The stability of the impedance matrix is evaluated by computing the condition number. The condition number depends on the number of segments used in the model; it

5

does not depend on the number of basis functions used on each segment. This formulation of the impedance matrix is compared to the polynomial numerical code developed by Djordjevic et al. (1990).

Section 9 gives the summary and the conclusions. A list of variables and their definitions is given in appendix B.

2 NUMERICAL RESULTS

The stability and convergence of our numerical algorithm is illustrated with the numerical calculations for a dipole. The admittance of the dipole calculated by using our algorithm is compared to the analytic approximation of King (1956). A 4- and 8-segment dipole models give almost identical admittances over a wide range of frequencies. Detailed convergence tests are also run for seven different models at the resonance and antiresonance of the dipole. These results are compared to King's (1956) results. The numerically calculated charge distribution is compared to the static-charge distribution for electrically small dipoles.

The dipole is described by three parameters: the total length, $2h = 1m$; the wire radius, $a = 4.5401E-5$; and the gap at the feed point, $d = 0$. In King's (1956) notation, Ω is 20, where $\Omega = 2 \ln(2h/a)$. Each arm of the dipole is divided into R segments. The program uses the symmetry of the dipole to eliminate the unknowns on one arm of the dipole. The algorithm can use one to seven basis functions per segment.

Figure 2–1 plots the admittance for an 8-segment model with three basis functions per segment and King's (1956) admittance; the matrix size is 24×24. The results are in very close agreement. The convergence of the algorithm is illustrated by comparing the admittance computed with 4- and 8-segment models with three basis functions per segment; the matrix sizes are 12×12 and 24×24, respectively. In this model, a gap of $d = 0.01$ meters was used to eliminate the logarithmic singularity in the charge distribution. A constant current is used on the source segment in the gap. The admittance for 4- and 8-segment models is plotted in figure 2–2 as a function of dipole length measured in wavelengths. The 4-segment model uses a total of 8 segments to model both arms of the dipole. The numerical calculation uses only 2-segments per wavelength at a dipole length of four wavelengths. The error in the 2-segments-per-wavelength model is very small. The small difference between the two admittance curves is plotted in figure 2–3. The error increases

7
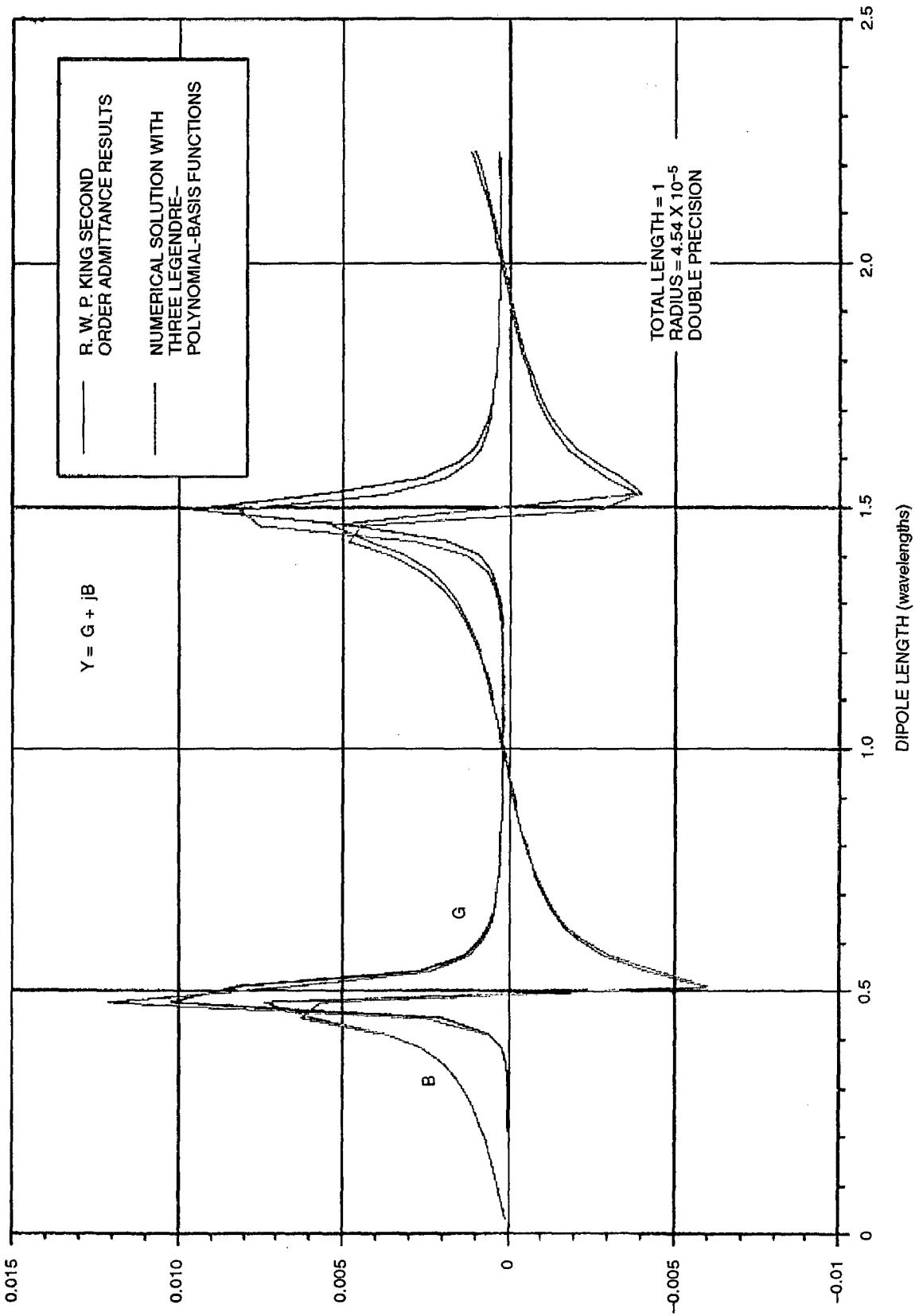
Figure 2-1. The dipole admittance calculated by R.W.P. King and the numerical model.

8
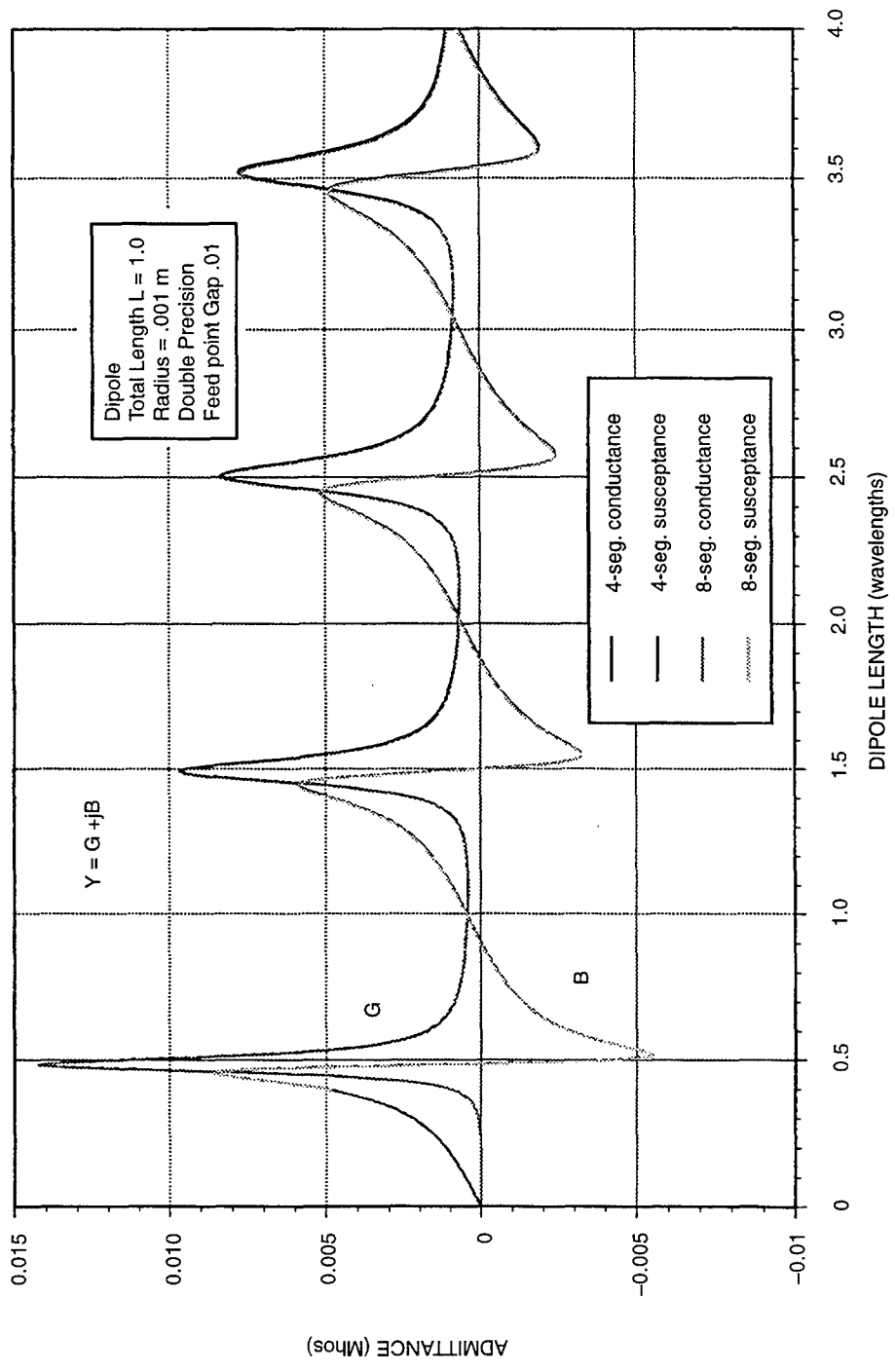
Figure 2-2. Admittance for a 4- and 8-segment models with three Legendre polynomials per segment.

9
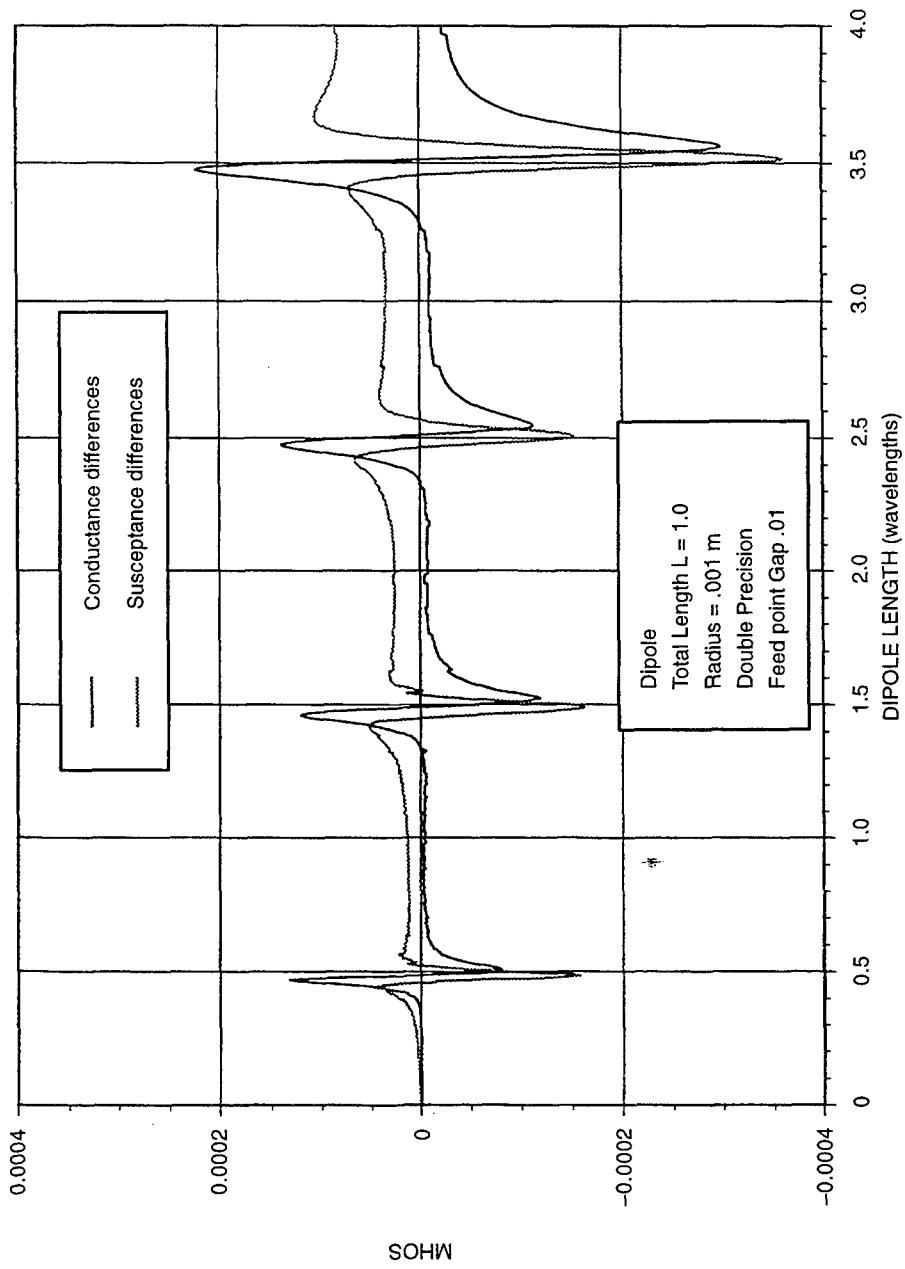
Figure 2-3. Difference in admittance for the 4- and 8-segment models with three Legendre polynomials per segment.

as fewer segments are used per wavelength.

The convergence of several dipole models is evaluated at the resonance frequency of the antenna. The resonance of a 1-meter dipole is at 146.0 MHz. The admittance is computed for one to seven basis functions per segment. The conductance and susceptance are plotted in figures 2–4 and 2–5 as functions of impedance matrix size. The size of the impedance matrix is determined by the number of unknowns used to model the charge distribution. The plot shows the results for three different charge distribution models: one, two, and seven basis functions per segment. The charge distribution models with three to six basis functions per segment are bound by the two and the seven basis function curves. The two and the seven basis function conductance curves are within 1% of King's (1956) computed result, the dotted line. The error in the one basis function conductance curve is less than 1% for nine or more segments. The percentage error for the susceptance cannot be computed. However, the error in the susceptance can be viewed as a phase error in the admittance. The phase error is less than 1.2° for the two and seven basis function susceptance curves. The phase error in the one basis function susceptance curve is less than 1° for the nine or more segments in the model. The three curves converge to the same conductance values, the typical difference in the conductance curves is 7/100% of King's (1956) value.

The convergence of several dipole models is also evaluated at the antiresonance frequency of the dipole. The antiresonance of a 1-meter dipole is at 281.51 MHz. The conductance and susceptance are plotted in figures 2–6 and 2–7 as functions of the impedance matrix size. The plot shows the results for three different charge distribution models: one, two, and seven basis functions per segment. The charge distribution models with three to six basis functions per segment are bound by the two and the seven basis function curves. The seven basis function conductance curves are within 3/10% of King's (1956) computed result, the dotted line. The two basis function conductance curves are within 3/10% of King's (1956) result when two or more segments are used in the model.

11
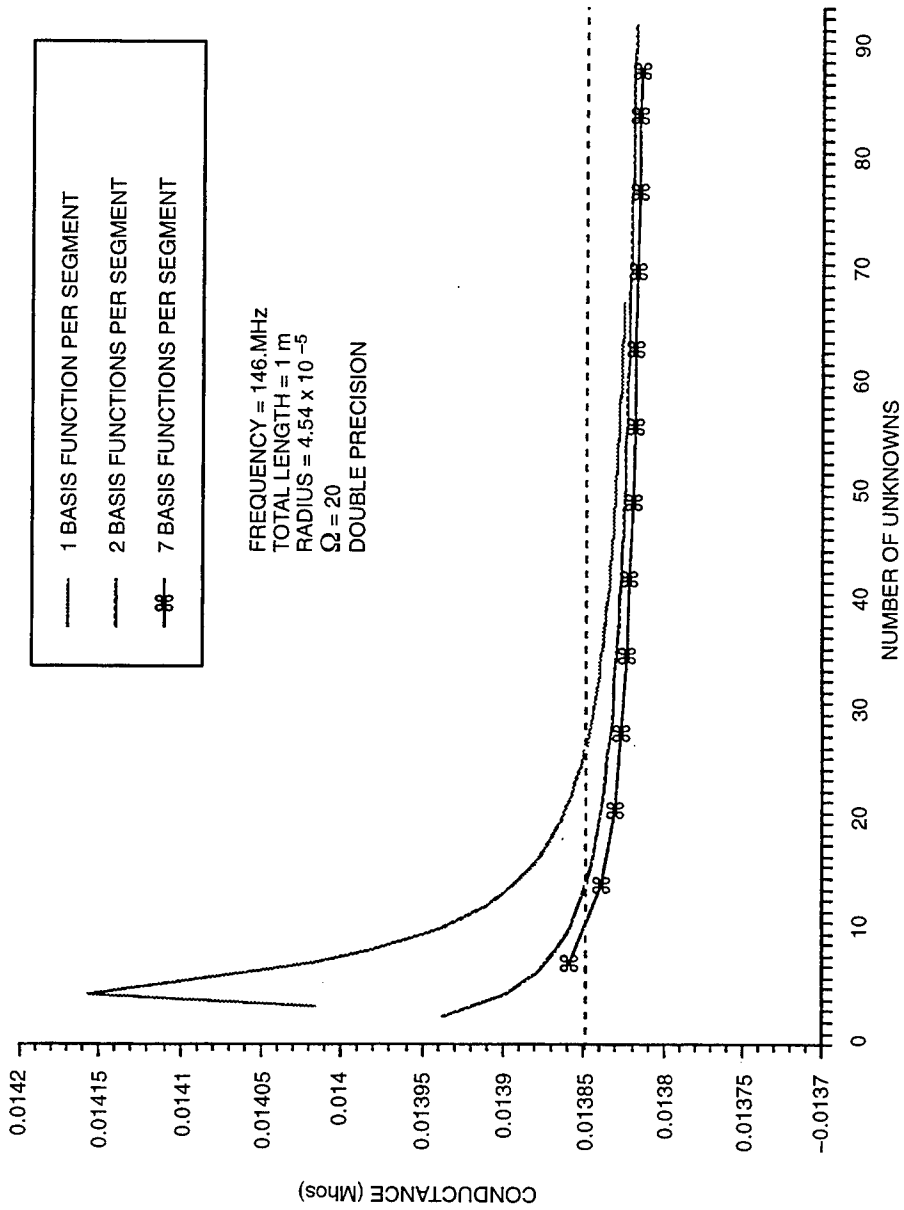
Figure 2-4. The three curves show the convergence of the conductance at resonance for one, two, and seven basis functions per segment.

Legend:
- 1 BASIS FUNCTION PER SEGMENT
- 2 BASIS FUNCTIONS PER SEGMENT
- 7 BASIS FUNCTIONS PER SEGMENT

FREQUENCY = 146.MHz
TOTAL LENGTH = 1 m
RADIUS = 4.54×10^{-5}
$\Omega = 20$
DOUBLE PRECISION

CONDUCTANCE (Mhos)

0.0142
0.01415
0.0141
0.01405
0.014
0.01395
0.0139
0.01385
0.0138
0.01375
−0.0137

NUMBER OF UNKNOWNS

0   10   20   30   40   50   60   70   80   90
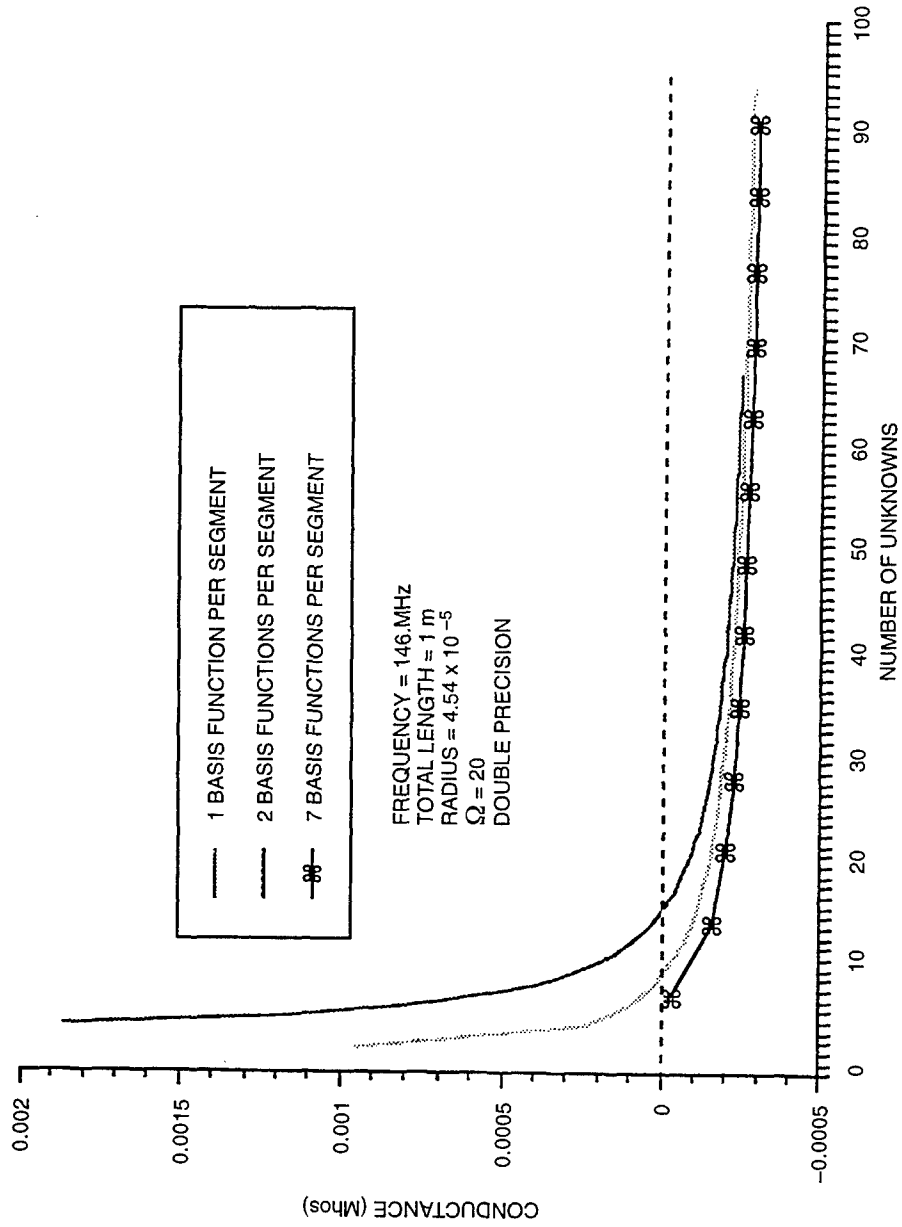
Figure 2-5. The three curves show the convergence of the susceptance at resonance for one, two, and seven basis functions per segment.

13
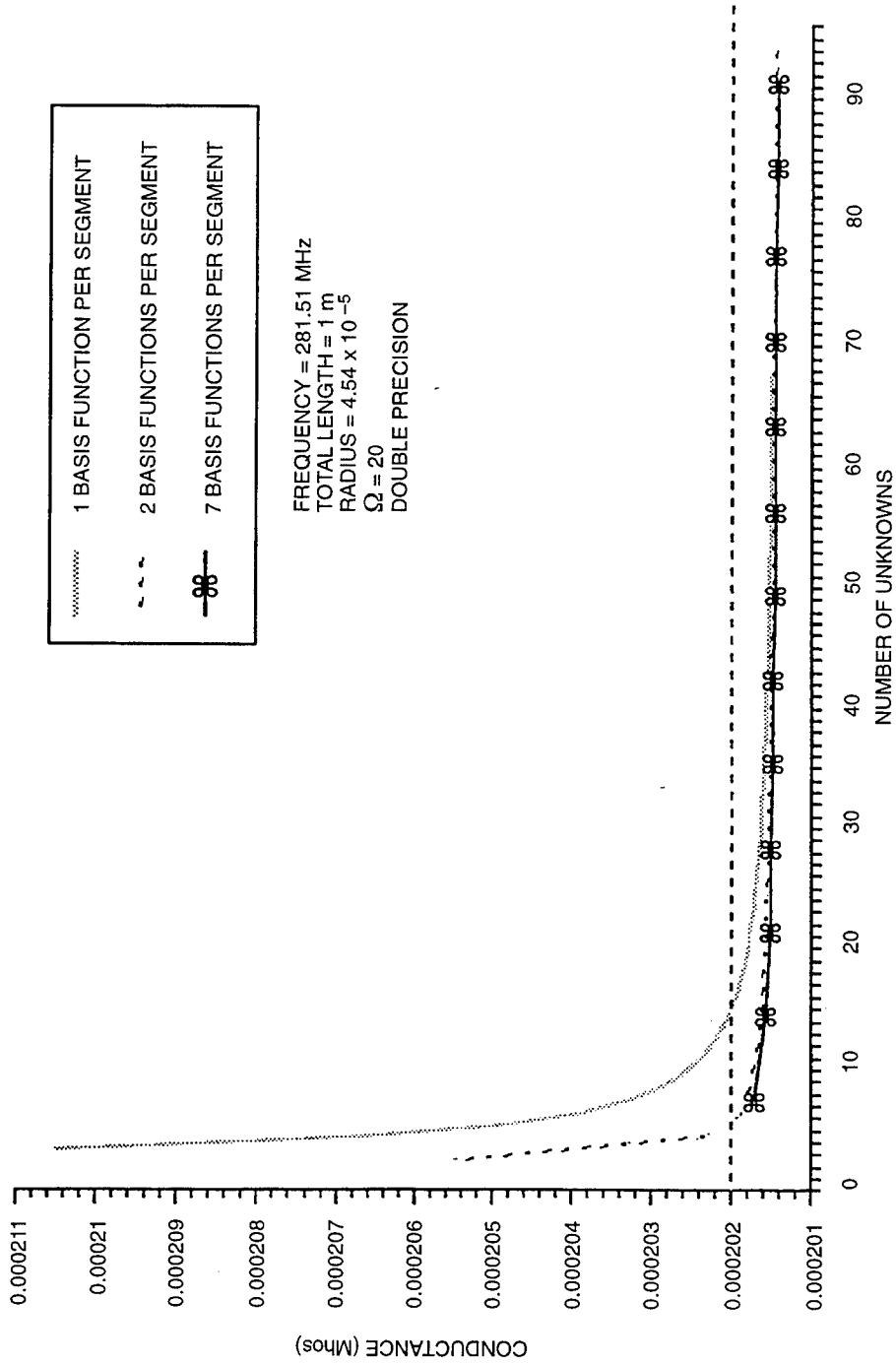
Figure 2-6. The three curves show the convergence of the conductance at antiresonance for one, two, and seven basis functions per segment.

14
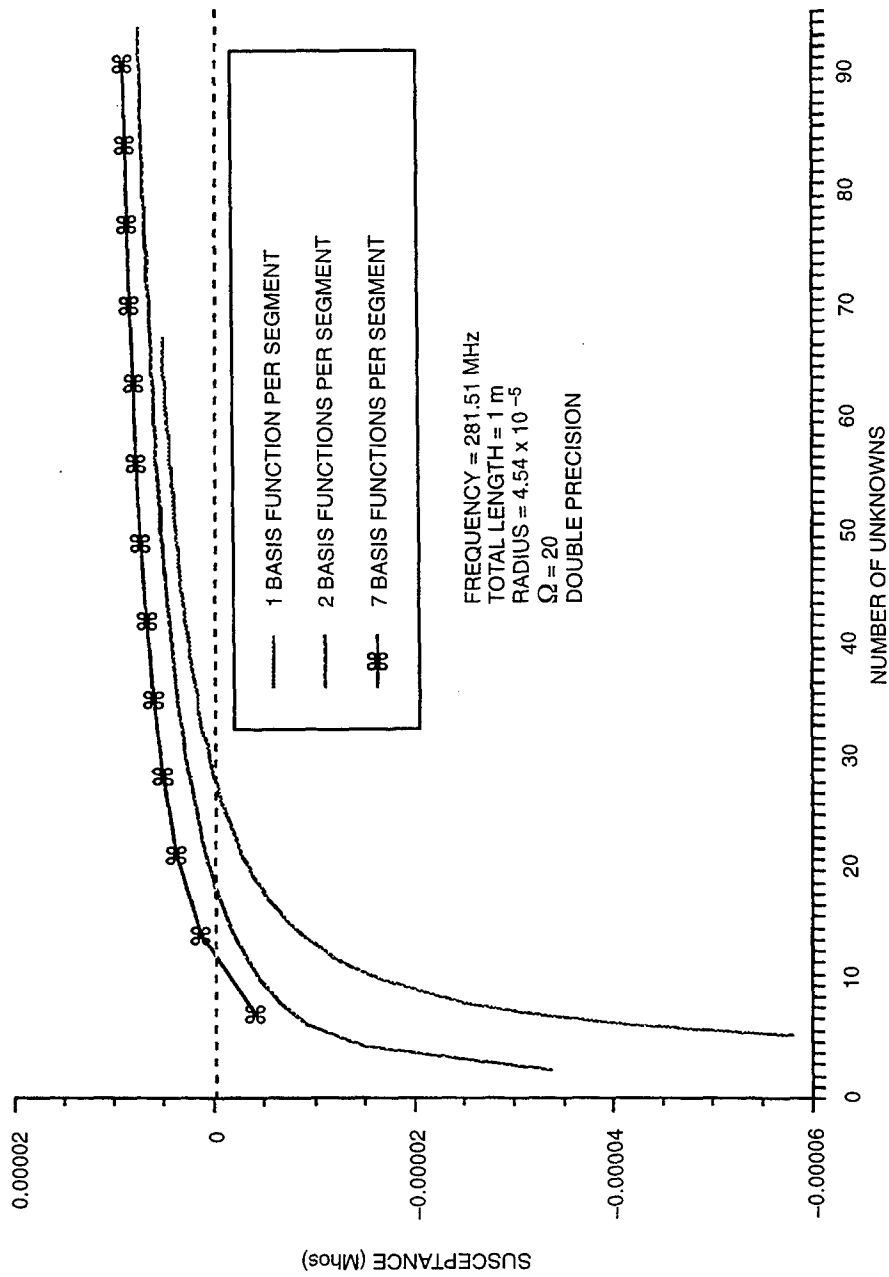
Figure 2-7. The three curves show the convergence of the susceptance at antiresonance for one, two, and seven basis functions per segment.

15

The error in the one basis function conductance curve is less than 1% for six or more segments. The phase error is less than 2.6° for the one, two, and seven basis function susceptance curves when 14, 3, and 1 or more segments are used in the respective models. The three curves converge to the same conductance values; the typical difference in the conductance curves is 3/100% of King's (1956) value.

The above plots indicate that the current converges at the feed point. The current at the feed point determines the net charge ($j\omega$) in each arm of the antenna; however, the charge distribution could be incorrect. The convergence of the charge distribution is a very sensitive test of the stability of our model. In our model, the charge distribution at the junction of two segments is not required to be continuous. A discontinuity in the charge distribution would create an error in the boundary condition. The magnitude of the discontinuity in the charge distribution is a good test of the accuracy of the solution. Several different polynomial models were tested for convergence and accuracy.

The charge distribution for an electrically small dipole was given in Watt (1967). In the following plots, the feed point is at 0 and the end of the wire is at 0.5. Figure 2–8 shows the results for a two-basis function model of the charge distribution with 12- and 24-segments, for a total of 24 and 48 unknowns, respectively. The charge distribution in the interior segments is continuous. On the feed point and end segment, the error in the linear charge distribution model can be approximated with a quadratic charge distribution. This quadratic charge distribution gives a quadrupole error in the potential surrounding the segment. The charge distribution error on the feed point and end segment does not affect charge distribution on the adjacent segment. The agreement between the 12- and 24-segment models shows that the algorithm converges as the number of segments is increased. The accuracy of the feed point and end segment is improved by using high-order polynomial models. Figure 2–9 shows results for a 3- and 6-segment model with eight basis

16
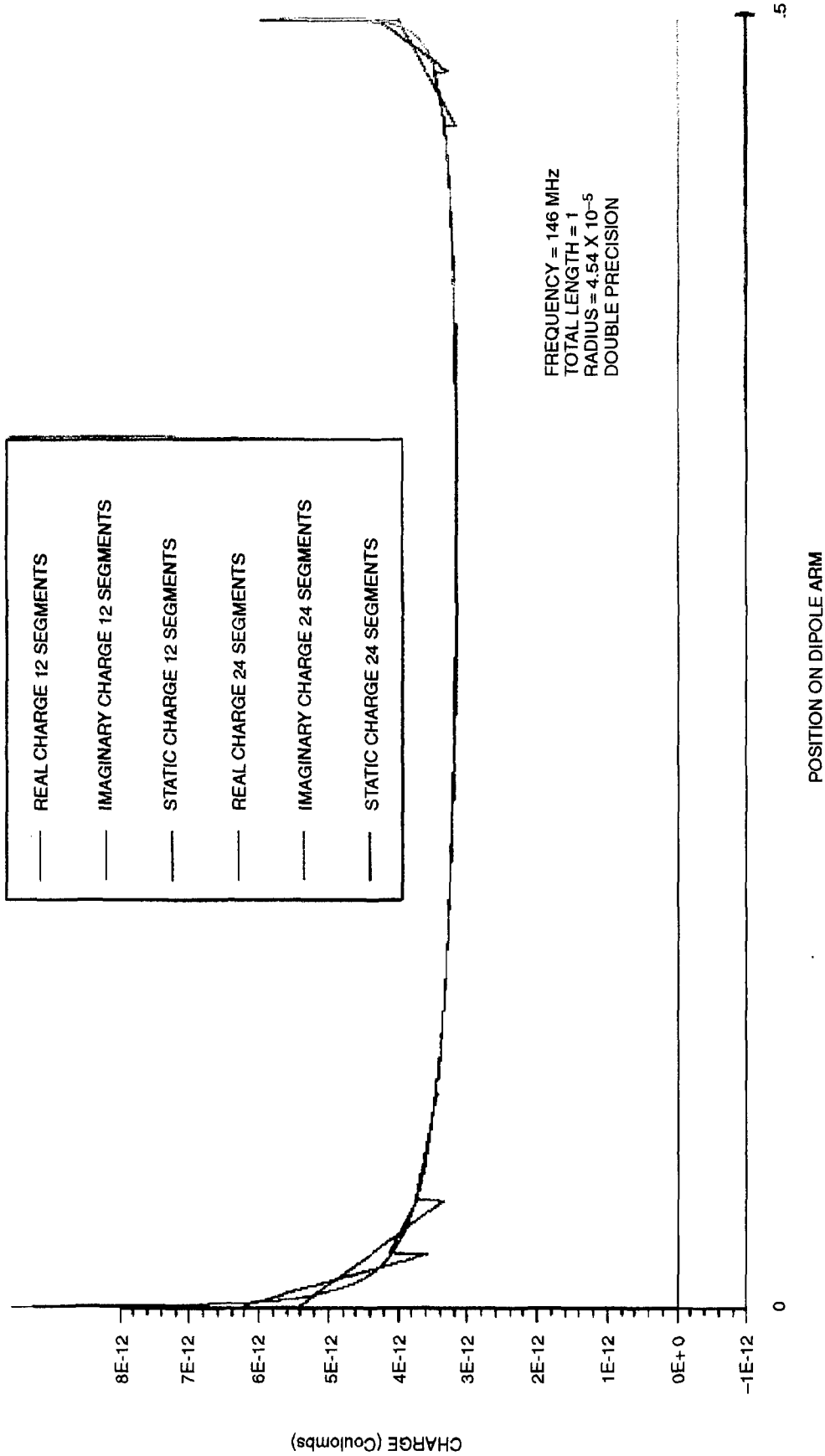
Figure 2-8. Charge distribution on an electrically small dipole modeled with 12 and 24 segments and two charge basis functions per segment.

FREQUENCY = 146 MHz
TOTAL LENGTH = 1
RADIUS = 4.54 X 10^{-5}
DOUBLE PRECISION

Legend:
- REAL CHARGE 12 SEGMENTS
- IMAGINARY CHARGE 12 SEGMENTS
- STATIC CHARGE 12 SEGMENTS
- REAL CHARGE 24 SEGMENTS
- IMAGINARY CHARGE 24 SEGMENTS
- STATIC CHARGE 24 SEGMENTS

CHARGE (Coulombs)

POSITION ON DIPOLE ARM

17
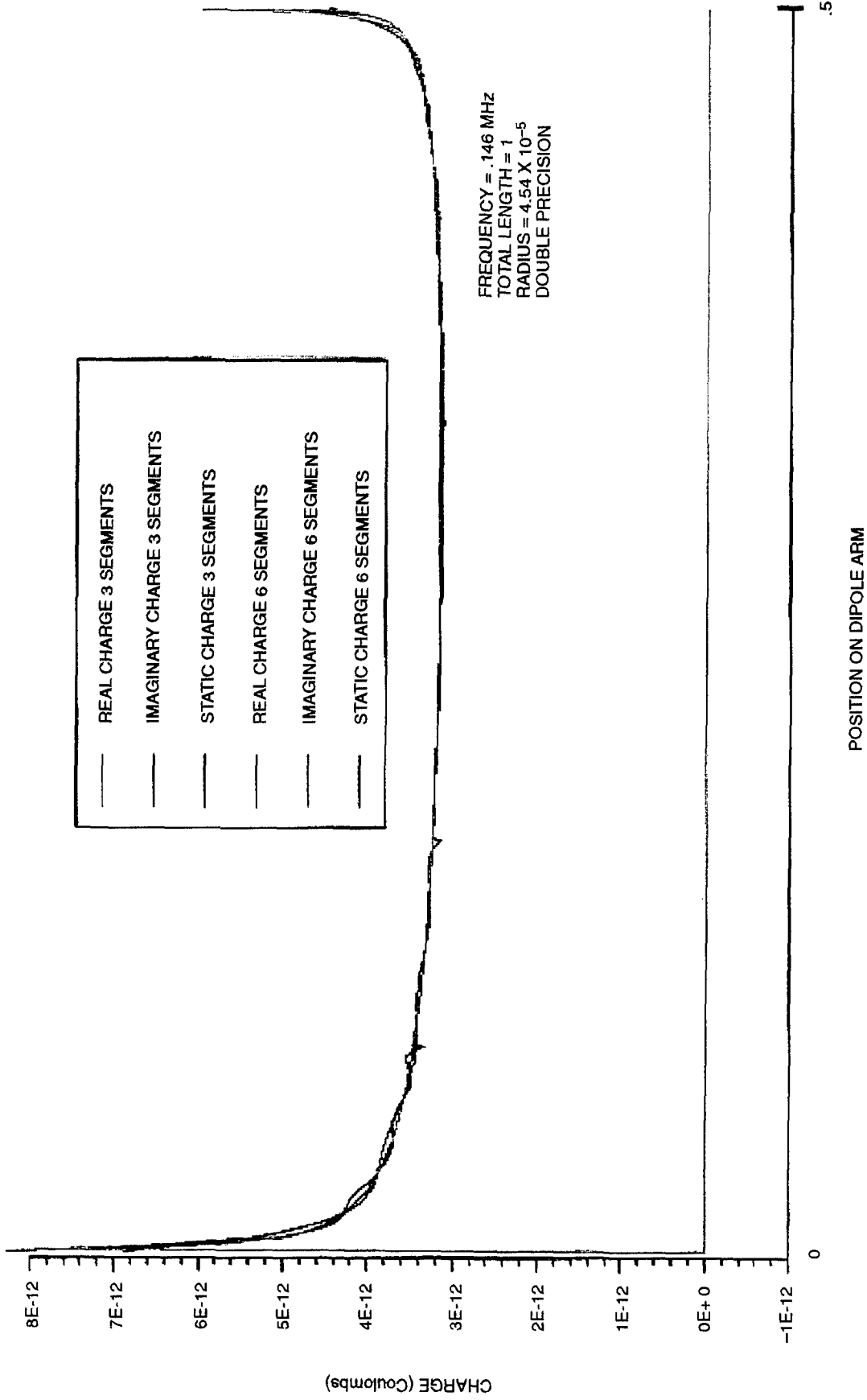
Figure 2-9. Charge distribution on an electrically small dipole modeled with 3 and 6 segments and eight basis functions per segment.

functions per segment[2], for a total of 24 and 48 unknowns, respectively. The error at the feed point and end segment is much smaller in this model. At the junction of the segments, the charge distribution has a small jump in value. The small difference between the 3- and 6-segment models illustrates how the solution converges as the number of segments is increased.

The accuracy of the model at the end of the wire can be improved by using more segments. Figure 2–10 shows the charge distribution at the end of the wire; the model uses 12 segments with seven basis functions per segment or a 84×84 matrix. This model is very accurate near the end of the antenna. The accuracy of the model at the end of the wire is attributed to the boundary condition, which is applied to the entire segment.

The plots of the charge distribution indicated a very stable algorithm. The errors on the feed point and end segment do not affect neighboring segments. This stability can be attributed to the boundary condition used in this algorithm.

---

2. The 8-segment model neglected the current term for the eight basis function. For electrically small antennas the error is insignificant.
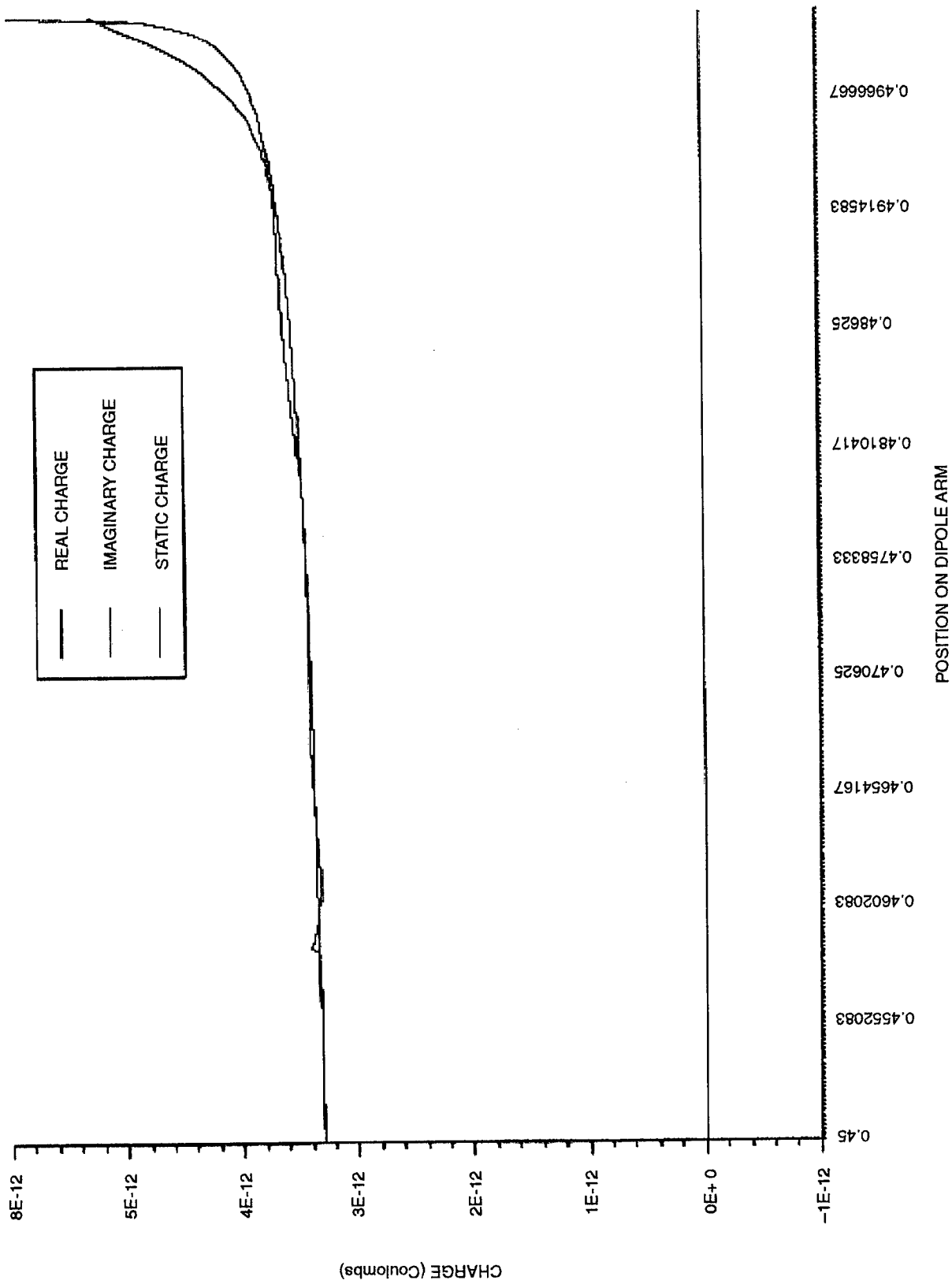
Figure 2-10. Charge distribution near the end of an electrically small dipole modeled with 12 segments and seven basis functions per segment.

3 ELECTROMAGNETIC EQUATIONS AND NOTATION

The algorithm solves for the current and charge distributions caused by an input voltage at the feed point of the antenna. The algorithm is implemented for a dipole antenna with a length, 2h, and a wire radius, a. The dipole is fed at the center with a single-frequency voltage source. The current flow at the feed point creates a buildup of charge on each arm of the antenna. The charge on the antenna moves in response to the parallel component of the electric field on the surface of the wire. On a perfect conductor, the charge moves to eliminate the parallel component of the electric field. The algorithm developed in this report could be used to model symmetric thin-wire antennas without closed loops.

The continuous charge distribution on the dipole is modeled in the computer with a finite number of basis functions. Each arm of the dipole is divided into R segments with a length, $L = h/R$ (figure 3–1). Segment 1 is at the feed point, and segment R is at the end of the wire. The position on each segment, s, is parameterized by t_s, where $-1 \leq t_s < 1$, t_s increases in the direction of increasing s. The charge and vector current distributions on segment s are modeled with N basis functions, $Q_{s\,n}(t_s)$ and $J_{s\,n}(t_s)$, respectively. The italic subscript s indicates the segment number, and the latin subscript n identifies the basis function number. Bold italic variables indicate a vector quantity. The unit vector, $\hat{u}_s$, for each segment, lies on the axis of the segment and points in the direction of increasing t_s. The current basis function, $J_{s\,0}(t_b)$, overlaps with the adjacent segment, $b = s - 1$. In terms of the basis functions, the charge and current distributions are approximated as follows:

$$Q_s(t_s) \simeq \sum_{n=0}^{N-1} \eta_{s\,n} Q_{s\,n}(t_s),$$

(3–1)

21
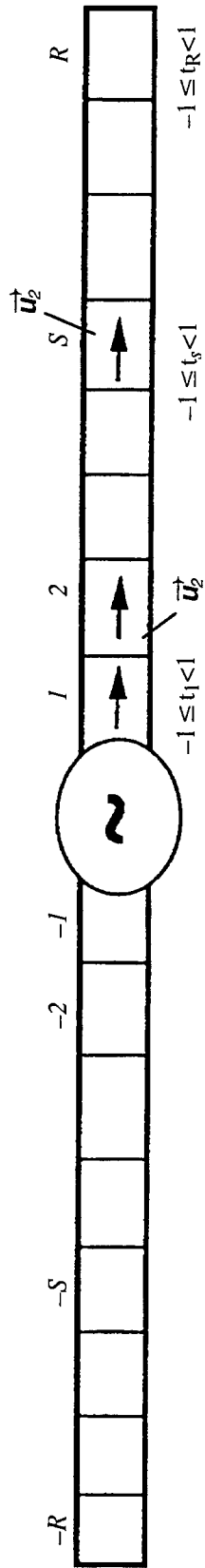
Figure 3-1. Each arm of the dipole is divided into R segments. The s segment is parameterized with t_s, where $-1 < t_s \leq 1$. The unit vector, $\boldsymbol{u}_s$, points in the direction of increasing t_s.

$$J_s(t_b) \simeq \sum_{n=0}^{N-1} \delta_{s\,n} J_{s\,n}(t_b) \quad \text{for } b = s-1 \text{ and } s. \tag{3-2}$$

The current is zero at the free end of each wire in the antenna. Equation (3-2) must vanish at the end of the wire. The current coefficients, $\delta_{s\,n}$, and charge coefficients, $\eta_{s\,n}$, are related by

$$\rho = -\frac{\nabla \cdot J}{j\,\omega}. \tag{3-3}$$

The continuity equation can be used to reduce 2N unknowns to N unknowns for each segment of the thin wire. The symmetry of the charge and current distributions is used to eliminate the unknowns on the left arm of the dipole.

The scalar potential, $\phi_{s\,n}(r)$, and vector potential, $A_{s\,n}(r)$, for each basis function is computed with the free-space Green's function:

$$\phi_{s\,n}(r) = \frac{1}{4\pi\epsilon_0} \int_{V'} Q_{s\,n}(r') \frac{e^{-jk|r-r'|}}{|r-r'|} dV', \tag{3-4}$$

$$A_{s\,n}(r) = \frac{1}{4\pi c^2 \epsilon_0} \int_{V'} J_{s\,n}(r') \frac{e^{-jk|r-r'|}}{|r-r'|} dV', \tag{3-5}$$

where r is the position of the field point, r' is the position of the source, $|r-r'|$ is the distance from source to the field point, and k is the wave number of the exciting signal. The free-space Green's function is a point source solution of Maxwell's equations. The Green's function is integrated over the region containing the source of the field r', $\rho(r')$, and $J(r')$. The units are chosen as rationalized (MKS), in free space, $1/(4\pi\epsilon_0)$ is $10^{-7}c^2$.

The scalar and vector potential solutions to Maxwell's equations are

$$\nabla^2 \phi + \frac{\omega^2}{c^2} \phi = -\frac{\rho}{\epsilon_0} \qquad (3\text{--}6)$$

and

$$\nabla^2 A + \frac{\omega^2}{c^2} A = -\frac{J}{\epsilon_0 c^2} \, . \qquad (3\text{--}7)$$

The Lorentz gauge condition is

$$c^2 \nabla \cdot A - j\omega\phi = 0. \qquad (3\text{--}8)$$

The Lorentz gauge condition has been used to simplify the current term (Feynman, Leighton and Sands, 1964) on the right side of equation (3–7). Equations (3–6) and (3–7) relate the potentials to the general charge and current distributions, ρ and J, where ρ and J obey the continuity equation (3–3).

The charge and current distributions, ρ and J, are determined indirectly with an electric-field boundary condition. The electric field for perfect conductors must be normal to the conducting surface. On each arm of the antenna, the parallel component of the electric field is zero on the surface. At the feed point, the input voltage is represented as a parallel component of the electric field.

The error in the boundary condition is the line integral of the electric field from the center of the feed point, $z = 0$, to the point t_f on segment f:

$$\text{EMF}(t_f) = \int_0^{z(t_f)} E \cdot dz = \phi(0) - \phi(t_f) - j\omega \int_0^{z(t_f)} A(z) \cdot dz \, . \qquad (3\text{--}9)$$

24

The subscript f denotes the field point on the field segment. The potentials, $\phi(t_f)$ and $A(z)$, are calculated with equations (3–4) and (3–5). The approximations used in the charge and current basis functions introduce errors in the $\text{EMF}(t_f)$:

$$\text{EMF}(t_f) = \sum_{s=1}^{R} \sum_{n=0}^{N-1} \left[\left[\phi_{s\,n}(0) - \phi_{s\,n}(t_f) \right] \eta_{s\,n} - j\omega \int_{0}^{z(t_f)} \delta_{s\,n} A_{s\,n}(z) \cdot dz \right].$$

(3–10)

Equation (3–10) relates the current and charge distributions on the source segment s to the electromotive force (EMF) on field segment f. Ideally, this integral is a constant equal to half of the feed-point voltage for a dipole. In practice, the continuous boundary condition is approximated by a discrete model.

The boundary condition on each segment is imposed by expanding the $\text{EMF}(t_f)$, equation (3–10), on segment f as a sum of Legendre polynomials

$$\text{EMF}(t_f) = \sum_{m=0}^{N-1} \alpha_{f\,m} P_m(t_f).$$

(3–11)

The N boundary conditions for each segment are imposed by setting the expansion constants equal to

$$\alpha_{f0} = \tfrac{1}{2} V_{in}$$

and

$$\alpha_{f\,m} = 0 \qquad \text{for } 0 < m < N.$$

(3–12)

25

In equation (3–13), the integral on the right is set equal to the constant, α_{fm}, defined in equation (3–12):

$$\alpha_{fm} = (m+\tfrac{1}{2})\int_{-1}^{1} P_m(t_f)EMF(t_f)dt_f. \qquad (3\text{--}13)$$

Equation (3–13) represents N boundary conditions for segment f. The total number of boundary conditions for the antenna is $R\cdot N$.

Equation (3–10) is substituted into equation (3–13) to give an $R\cdot N \times R\cdot N$ interaction matrix:

$$\alpha_{fm} = (m+\tfrac{1}{2})\int_{-1}^{1} P_m(t_f) \sum_{s=1}^{R} \sum_{n=0}^{N-1} \left[\left[\phi_{s\,n}(0) - \phi_{s\,n}(t_f)\right]\eta_{s\,n} - j\omega \int_{0}^{z(t_f)} \delta_{s\,n} A_{s\,n}(z)\cdot dz \right] dt_f. \qquad (3\text{--}14)$$

The continuity equation (3–3) is used to eliminate either $\delta_{s\,n}$ or $\eta_{s\,n}$ from the above equation. Each boundary condition is a function of the N basis function coefficients, $\delta_{s\,n}$ or $\eta_{s\,n}$.

Equation (3–14) is a matrix equation:

$$\alpha_{fm} = Z_{fs\,mn}\chi_{s\,n}, \qquad (3\text{--}15)$$

where $\chi_{s\,n} = \delta_{s\,n}$ or $\eta_{s\,n}$. The elements in the matrix, $Z_{fs\,mn}$, will have units of impedance when $\chi_{s\,n} = \delta_{s\,n}$ and capacity when $\chi_{s\,n} = \eta_{s\,n}$. The total number of unknowns is $R\cdot N$. A combination of $\delta_{s\,n}$ and $\eta_{s\,n}$ is used to model the current and charge distribution. For simplicity, the complete matrix will be called the impedance matrix.

4 BASIS FUNCTIONS

Harrington (1968) was the first to formulate the electromagnetic problem in the method of moments. In his approach, each wire in the antenna is divided into several segments and the charge and current distributions on each segment of the antenna are modeled with square pulses. As a result, both the current and charge distributions are discontinuous. The current model can be made continuous by introducing triangular current pulses; however, the charge distribution remains discontinuous. A smooth charge distribution can be modeled by introducing extra current and charge basis functions. These basis functions provide a more realistic model of the charge distribution on a wire.

The first current basis function is a triangular basis function that gives a square-pulse charge distribution. The triangular basis function shown in figure 4–1(row b) has been used by many authors (Michalski and Butler, 1983; Hwu and Wilton, 1988). The triangular basis function, $J_{s\,0}(t_f)$, overlaps the two segments $s-1$ and s:

$$J_{s\,0}(t_{s-1}) = -\frac{j\omega}{2}(1 + t_{s-1})\hat{u}_{s-1}, \qquad (4\text{–}1a)$$

$$J_{s\,0}(t_s) = -\frac{j\omega}{2}(1 - t_s)\hat{u}_s, \qquad (4\text{–}1b)$$

$$J_{s\,0}(t_f) = 0 \text{ for } f \neq s-1 \text{ or } s. \qquad (4\text{–}1c)$$

The continuity equation (3–3) is used to compute the charge distribution, $Q_{s\,J}(t_b)$ for $J_{s\,0}$:

$$Q_{s-1\,J}(t_{s-1}) = 1/L, \qquad (4\text{–}2a)$$

$$Q_{s\,J}(t_s) = -1/L, \qquad (4\text{–}2b)$$

CURRENT	CHARGE	SPATIAL DEPENDENCE OF POTENTIAL	
		STATIC PART	FAR FIELD
a.		$1/r$	$1/r$
b.		DIPOLE $1/r^2$	Lk/r
c.		QUADRAPOLE $1/r^3$	$(LK)2/r$
d.		OCTOPOLE $1/r^4$	$(LK)3/r$
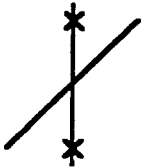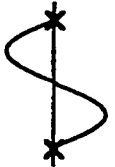
Figure 4-1. The current and charge basis functions where the segment length is L and the wave number is k.

28

$$Q_{s\,J}(t_f) = 0 \ \text{ for } f \neq s \text{ or } s-1. \tag{4-2c}$$

The charge distribution described by equation (4–2) is a portion of the charge distribution on the segment s. The complete model of the charge distribution on the segment s uses two triangular pulses, $J_{s\,0}(t_s)$ and $J_{s+1\,0}(t_s)$. The total charge on the segment, $Q_s(t_s)$, is

$$Q_s(t_s) = \left[\frac{\delta_{s+1\,0} - \delta_{s\,0}}{L} \right], \tag{4-3}$$

which is equivalent to

$$Q_s(t_s) = \eta_{s\,0} Q_{s\,0}(t_s) \tag{4-4a}$$

where

$$\eta_{s\,0} = \left[\frac{\delta_{s+1\,0} - \delta_{s\,0}}{L} \right] \ \text{ and } \ Q_{s\,0}(t_s) = P_0(t_s) \ \text{ for } -1 \leq t_s \leq 1. \tag{4-4b}$$

$P_0(t_s)$ is the first Legendre polynomial with the standard parameterization, $P_n(1) = 1$. The constant, $\eta_{s\,0}$, is the derivative of the triangular current basis functions.

The charge and current distribution created by the first current basis function, $J_{s\,0}(t_s)$, can be parameterized with either $\delta_{s\,0}$ or $\eta_{s\,0}$. Equations (4–1) and (4–4) are simple functions of $\delta_{s\,0}$ and $\delta_{s-1\,0}$. The converse is not true; the $\delta_{s\,0}$ are complex functions of $\eta_{s\,0}$. The $\delta_{s\,0}$ are calculated by integrating the continuity equation. Each $\delta_{s\,0}$ is the sum of $\eta_{b\,0}$ for different segments. The sum is constrained to be zero at the end of the wire. The $\delta_{s\,0}$ give the simplest description of the first charge basis function.

The higher order current basis functions modify the current in the interior of the segment s without changing the current at the ends of the segment. The second current basis function is a quadratic polynomial on the segment, which is zero at the ends and outside the segment (figure 4–1, row b). The third basis function is a cubic polynomial, which is zero at the center of the segment, at the ends of the segment, and outside the segment (figure 4–1, row c). In general, the nth order current basis function is an n+1 order polynomial, which is zero at n–1 interior points on the segment, at the ends of the segment, and outside the segment. However, the locations of the n–1 interior zeros is not obvious (figure 4–1, row d). On the other hand, the charge basis functions (figure 4–1, column 2) computed from the continuity equation, are proportional to the Legendre polynomials.

In the general case, the charge basis functions are Legendre polynomials on the interior of the segment and zero outside the segment (figure 4–1, column 2). The charge distribution on the segment is approximated by N charge basis functions:

$$Q_s(t_s) = \frac{-\delta_{s0}}{L} P_0(t_s) + \sum_{n=1}^{N-1} \eta_{sn} P_n(t_s), \tag{4-5}$$

$$Q_s(t_{s-1}) = \frac{\delta_{s0}}{L} P_0(t_{s-1}).$$

The current distribution is calculated from the continuity equation and equation (4–5). The following relations are identities for Legendre polynomials for all t:

$$\int_{-1}^{t} P_0(p)dp = [P_0(t) + P_1(t)] \quad \text{for } n = 0, \tag{4-6}$$

30

$$\int_{-1}^{t} P_n(p)dp = \frac{1}{2n+1}[P_{n+1}(t) - P_{n-1}(t)] \quad \text{for } n > 0, \tag{4-7}$$

$$P_n(t) = \frac{1}{2^n n!} \frac{d^n}{dt^n}(t^2-1)^n \quad \text{for } n \geq 0. \tag{4-8}$$

Equations (4–6) and (4–7 for n=1) are verified by direct calculation. In the general case, equation (4–7) is differentiated and simplified with the equation (4–8) (Gradshteyn and Ryzhik, 1980):

$$P_n(t) = \frac{1}{2n+1}\left[\frac{1}{2^{n+1}(n+1)!}\frac{d^{n+2}}{dt^{n+2}}(t^2-1)^{n+1} - \frac{1}{2^{n-1}(n-1)!}\frac{d^n}{dt^n}(t^2-1)^{n-1}\right]. \tag{4-9}$$

For $n \geq 2$, this equation can be rewritten

$$P_n(t) = \frac{1}{(2n+1)2^{n+1}(n+1)!}\frac{d^n}{dt^n}\left[\frac{d^2}{dt^2}(t^2-1)^{n+1} - 4(n+1)n(t^2-1)^{n-1}\right]. \tag{4-10}$$

The second derivative is evaluated to give

$$P_n(t) = \frac{1}{(2n+1)2^{n+1}(n+1)!}\frac{d^n}{dt^n}\left[\left[4(n+1)nt^2 + (n+1)2(t^2-1) - 4(n+1)n\right](t^2-1)^{n-1}\right]. \tag{4-11}$$

The three terms combine to give

$$P_n(t) = \frac{1}{(2n+1)2^{n+1}(n+1)!} \frac{d^n}{dt^n}\left[(n+1)(4n+2)(t^2-1)^n\right] = \frac{1}{2^n n!}\frac{d^n}{dt^n}(t^2-1)^n.$$

(4–12)

The current basis functions computed from the continuity equation (3–3) are

$$J_{s\,n}(t_s) = -\frac{j\omega L}{4n+2}[P_{n+1}(t_s) - P_{n-1}(t_s)]\,\hat{u}_s \quad \text{for } n > 0,$$

(4–13a)

and

$$J_{s\,n}(t_f) = 0 \quad \text{for } f \neq s.$$

(4–13b)

These current basis functions modify the current in the interior of the segment without changing the current at the ends of the segment.

The current on the segments s and $s-1$ is approximated by N current basis functions

$$J_s(t_s) = -\frac{j\omega}{2}(1 - t_s)\delta_{s\,0}\hat{u}_s - \sum_{n=1}^{N-1} \frac{j\omega L}{4n+2}[P_{n+1}(t_s) - P_{n-1}(t_s)]\hat{u}_s \eta_{s\,n},$$

(4–14a)

and

$$J_s(t_{s-1}) = -\frac{j\omega}{2}(1 + t_{s-1})\delta_{s\,0}\,\hat{u}_{s-1}.$$

(4–14b)

Equation (4–14) models the current on the wire as a continuous function of t. The triangular basis function creates a piecewise linear approximation of the current. The higher order basis functions represent the difference between the current distribution and

the piecewise linear approximation of the current distribution. For a slowly changing function, the approximation error goes to zero as the segment length, L, is decreased.

The charge basis functions model the charge distribution on each segment as a continuous function. However, the charge distribution at the junction of two segments may not be a continuous function. In nature, this problem does not occur; the electric field at the discontinuity would redistribute the charge to eliminate the discontinuity. The electric field boundary condition should create a continuous charge distribution. The charge distribution computed for the dipole, figures 2–8 and 2–9 in section 2, has a very small discontinuity between segments.

5 MULTIPOLE POTENTIALS OF THE BASIS FUNCTIONS

An exact model for the continuous charge distribution on a segment requires an infinite sum of Legendre polynomial basis functions. In our numerical model, only a fixed number, N, of charge basis functions can be used in the model. An error in modeling the charge distribution introduces errors in modeling the potentials. The error in the potential is discussed for three different regions: the far, intermediate, and near fields of the segment. These basis functions allow the errors in the potentials and in the charge distribution to be analyzed and modeled in detail.

The modeled far, intermediate, and near fields are the sum of the fields created by the individual basis functions. Each basis function contributes differently to the far, intermediate, and near fields of the antenna. The contribution to the three regions can be examined by expanding the free–space Green's function in a 1/r expansion (Jackson, 1975). In this section, the expansion of the free–space Green's function is limited to the axis of the segment. In the near field, the basis functions are multipole expansions of the charge distribution on a segment. In particular, the basis functions represent the monopole, dipole, quadrupole, octupole, etc., of the charge distribution. The potentials in the intermediate and far fields depend on the wavelength, λ, of the exciting frequency and segment length. The intermediate and far field terms are small for electrically small antennas. This approach is compared to the matrix transformation developed by Canning (1992).

Equation (3–4), without the constant $1/(4\pi\epsilon_0)$, is called the potential integral:

$$\kappa_{s\,n}(\boldsymbol{r}) = \int_{V'} P_{s\,n}(2z'/L)\frac{e^{-jk|\boldsymbol{r}-\boldsymbol{r'}|}}{|\boldsymbol{r}-\boldsymbol{r'}|}\,dV'. \tag{5-1}$$

The asymptotic form of the potential integral $\kappa_{s\,n}$ is found by expanding the Green's function in a $1/r$ series. The analysis of the integral is simplified by limiting its evaluation to the z-axis of the wire and setting a = 0. The potential integral, $\kappa_{s\,n}(z_0)$ on the z-axis, is found by replacing the quantity $|r-r'|$ in equation (5–1) with $|z_0-z|$, where z_0 is the distance to the center of the charge distribution, $P_n(2z/L)$, on the segment s :

$$\kappa_{s\,n}(z_0) = \int_{-L/2}^{L/2} P_n(2z/L) \frac{e^{-jk(z_0-z)}}{z_0-z} dz. \tag{5–2}$$

If $|L/2| \ll z_0$, the factors, $1/|z_0-z|$ and e^{jkz}, in the free-space Green's function are expanded in a power series of z/z_0 and jkz, respectively:

$$\kappa_{s\,n}(z_0) = e^{-jkz_0} \int_{-L/2}^{L/2} P_n(2z/L) \left[\sum_{k=0}^{\infty} \frac{z^k}{z_0^{k+1}} \right] \left[\sum_{p=0}^{\infty} j^p \frac{k^p z^p}{p!} \right] dz$$

$$\text{for } z_0 \gg L/2. \tag{5–3}$$

The terms with like power of z^m are collected together as:

$$\kappa_{s\,n}(z_0) = e^{-jkz_0} \sum_{m=0}^{\infty} \left[\sum_{p=0}^{m} \frac{j^p k^p}{p! z_0^{m-p+1}} \right] \int_{-L/2}^{L/2} P_n(2z/L) z^m dz, \tag{5–4}$$

where m = p+k. The integral can be simplified by making a change of variables $2z/L = t$:

$$\kappa_{s\,n}(z_0) = e^{-jkz_0} \sum_{m=0}^{\infty} \left[\sum_{p=0}^{m} \frac{j^p k^p (L/2)^{m+1}}{p! z_0^{m-p+1}} \right] \int_{-1}^{1} P_n(t) t^m dt. \tag{5–5}$$

36

The integral factor is independent of frequency and segment length. The integral can be evaluated by expanding t^m in terms of Legendre polynomials:

$$t^m = \sum_{q=0}^{m} \zeta_q^m P_q(t), \tag{5-6}$$

where $\zeta_q^m = 0$ for $q > m$. The integral reduces to

$$\int_{-1}^{1} P_n(t) t^m dt = \sum_{q=0}^{m} \zeta_q^m \int_{-1}^{1} P_n(t) P_q(t) dt. \tag{5-7}$$

The integration of the orthogonal Legendre polynomials gives

$$\int_{-1}^{1} P_n(t) t^m dt = \zeta_n^m / (n + \tfrac{1}{2}). \tag{5-8}$$

For $m < n$, $\zeta_n^m = 0$, the above integral vanishes; equation (5-5) simplifies to

$$\kappa_{s\,n}(z_0) = e^{-jkz_0} \sum_{m=n}^{\infty} \left[\sum_{p=0}^{m} \frac{j^p k^p (L/2)^{m+1}}{p! z_0^{m-p+1}} \right] \zeta_n^m / (n + \tfrac{1}{2}). \tag{5-9}$$

At very large distances from the segment, $z_0 \gg L$, most of the terms in equation (5-9) are small. For a fixed p, the largest term occurs for $m = n$. The terms with $m > n$ involve higher powers of $1/z_0$. The sum of the largest terms is

$$\kappa_{s\,n}(z_0) = e^{-jkz_0} \sum_{p=0}^{n} \frac{j^p k^p (L/2)^{n+1}}{p! z_0^{n-p+1}} \zeta_n^n / (n + \tfrac{1}{2}) \quad \text{for } z_0 \gg L. \tag{5-10}$$

37

Equation (5–10) exhibits the frequency and the $1/z_0$ dependence of the potential.

The term with p = 0 is independent of frequency k; it is, by definition, the near field part potential integral. The near field of $\kappa_{s\,n}$ falls off as $[L/2z_0]^{n+1}$. The nth basis function is the nth multipole expansion of the charge distribution on a segment. The intermediate field depends on the frequency, k, but falls off faster than $1/z_0$, n > p > 0. The intermediate field represents stored energy; they do not radiate energy to infinity. The term with p = n has a $1/z_0$ dependence; this term is the far field part of the potential. For the far field term, the coefficient of the $\zeta_n^n/(n+\frac{1}{2})$ simplifies to $j^n L/2[kL/2]^n/(n!z_0)$. The factor, kL/2, simplifies to $\pi L/\lambda$. These results are summarized in figure 4–1 (Static Part and Far Field columns).

Equation (5–10) has a simple physical interpretation. For a static-charge distribution, $P_n(t)$, the potential cancels at large distances so that it falls off as $1/z_0^{n+1}$. The frequency dependency of the Green's function *prevents* the potential integral from canceling in the far field[3]. This leads to frequency-dependent terms in the potential integral.

The above discussion is limited to the radial dependence of the potential integral. The angular dependence of the near field (static potential integral) is $P_n(\cos\theta)$, where θ is measured relative to the axis of the segment. For the case n = 0, the above discussion needs to be modified. The first current basis function yields two square-pulse charge basis functions, which form a dipole. As a result, the potential for the static-charge distribution created by the first current basis function falls off as $1/z_0^2$.

---

3. If the segment is the same size or larger than the wavelength, the opposite effect takes place. In this case, the phase term causes the potentials to constructively add to give a 1/r term for some of the basis functions. These basis functions could be used as entire basis functions; however, the higher order basis functions may not fall off as fast. In this case, the advantages of the basis functions would be lost.

In our approach, the far and intermediate fields are modeled by the net charge distribution, $P_0(t_f)$, on each segment. The high-order basis functions model the near field as independent degrees of freedom. The high-order basis functions also model the intermediate fields, which depend on the factor, $kL/2$ or $\pi L/\lambda$, in equation (5–10). For electrically small antennas, $(h < \lambda/4\pi)$, the constant, $\pi L/\lambda$, is small. Therefore, the frequency-dependent terms in the potential integral are small. The impedance matrix computed from these basis function has small frequency-dependent terms. The properties of the fields for electrically small antennas are explicit by the impedance matrix.

These basis functions allow the error to be discussed in detail. There are two types of errors in this model of the charge-distribution errors. The first error is introduced by using a finite number of charge basis functions to model the charge distribution. The second error is caused by the numerical evaluation of the charge basis functions coefficient, $\eta_{s\,n}$. Any error in the charge distribution creates an error in the potentials. However, for these basis functions, the impact of the errors in the potentials are limited to the near field around each segment. The error in the charge basis functions coefficient, $\eta_{s\,n}$, is determined by the electric field boundary condition, section 7. The detailed discussion of the local error on each segment is given in section 8.

These basis functions create a structured model of near, intermediate, and far fields; this simplifies the impedance matrix. The Canning (1992) used a matrix transformation technique to add structure to the impedance matrix. The matrix transformation creates oscillatory basis functions that model the charge distribution created by a scattering electromagnetic wave. When the oscillations in the charge distribution are larger than a wavelength, the oscillatory basis functions have directional radiation patterns. The directional radiation pattern simplifies the interaction between different segments. For an oscillation period smaller than a wavelength, the potentials are evanescent, i.e., the potentials decay exponentially in the radial direction from the segment. The matrix transformation will reduce the number of large elements in the impedance matrix. This simplifies the solution

of the impedance matrix. However, the accuracy of the solution depends on the accuracy of the algorithm used to compute the initial impedance matrix.

The algorithm developed in this report is designed to accurately compute the individual elements of the impedance matrix. The basis functions and boundary condition combine to create a high-order multipole error in the charge-distribution model. The admittance at resonance and antiresonance depends on the size of the matrix model. The higher order basis functions simplify the impedance matrix and improve the convergence of the algorithm.

In the above discussion, the wire radius was not included in the $1/z_0$ expansion of the potential. However, near the surface of the segment, the finite radius must be included in the calculation of the potential integral. The numerical calculation of the potential is discussed in section 6.

6 POTENTIAL INTEGRAL

The convergence of a numerical algorithm depends on the accuracy of the potential integral calculation. Approximations in the potential integral calculation can cause convergence and stability problems in the charge distributions at the end of the wire. These problems are discussed by Popovic B. D., M.B. Dragovic, and A. R. Djordjevic (1982). The potential integral, $\kappa_{s\,n}$ on the surface of the segment, was evaluated by Butler (1975) for constant and linear charge distributions. His method cannot be generalized for arbitrary basis functions, $P_n(s)$. The numerical algorithm developed in this section can calculate the potential integral, $\kappa_{s\,n}$, to any desired accuracy.

In section 5, the charge distribution was on a line, equation (5–1). In this section, the charge distribution will be a surface charge, $1/(2\pi a)P_n(Lz'/2)$, on the cylinder of radius a. The cylindrical coordinate system (figure 6–1) is used to compute the potential integral. The axis of the cylinder is the z–axis and the central cross section of the cylinder is in the x–y plane. The potential integral is evaluated at the point $r = (\rho,\ \varphi,\ z)$. The kernel has rotational symmetry about the z-axis; therefore, the equations are simplified by setting $\varphi = 0$. The integration is over the surface of the cylinder, $r' = (a,\ \varphi',\ z')$:

$$\kappa_n(\rho,z) = \frac{1}{2\pi}\int_0^{2\pi}\int_{-L/2}^{L/2} P_n(2z'/L)\frac{e^{-jk|r-r'|}}{|r-r'|}\,dz'\,d\varphi',\qquad (6\text{–}1)$$

where

$$|r-r'| = [(z-z')^2+\rho^2+a^2-2a\rho\cos\varphi']^{1/2}.$$

In this section, the subscript s will be dropped from the $\kappa_{s\,n}(r)$ and the charge distribution, $P_n(t_s)$. The kernel can be written as the sum of two parts: the singular part is
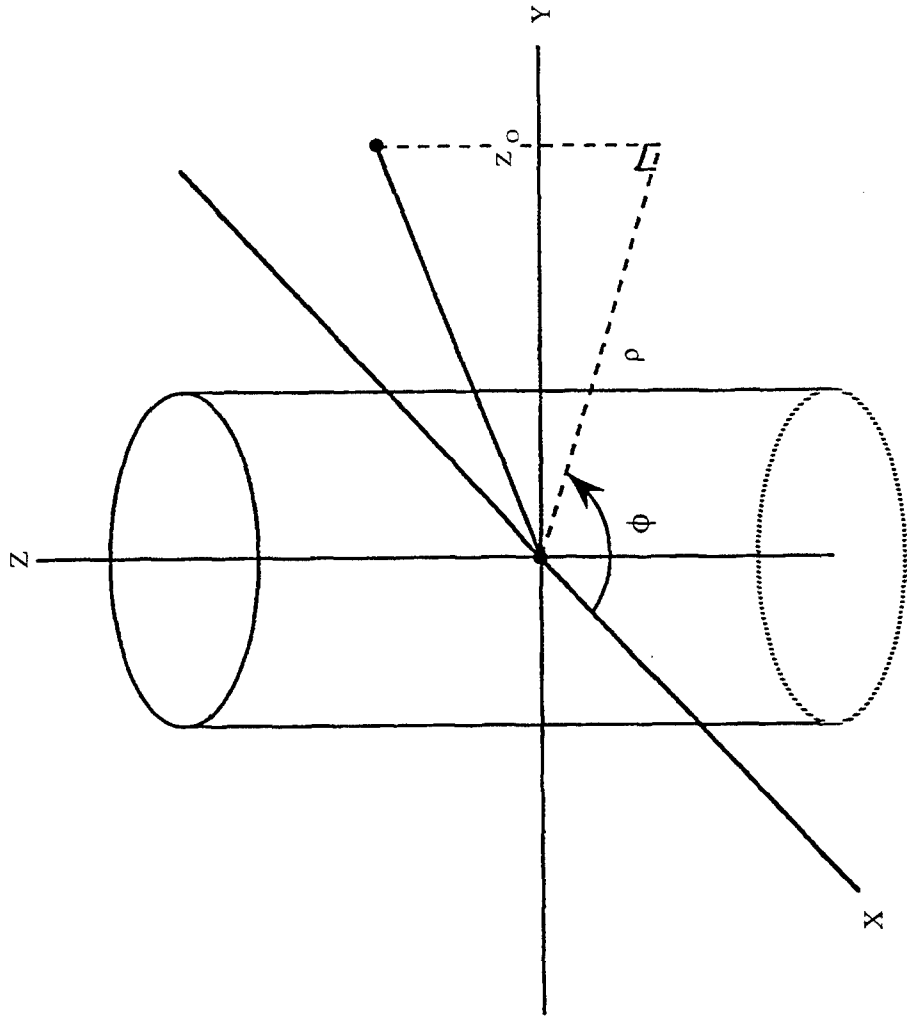
Figure 6-1. Coordinate system used to define the field point (ρ, ϕ, z).

$$\kappa_n^s(\rho,z) = \frac{1}{2\pi} \int_0^{2\pi} \int_{-L/2}^{L/2} P_n(2z'/L) \frac{1}{|\mathbf{r}-\mathbf{r'}|} \, dz' \, d\varphi', \qquad (6\text{--}2)$$

and the frequency-dependent nonsingular part is

$$\kappa_n^f(\rho,z) = \frac{1}{2\pi} \int_0^{2\pi} \int_{-L/2}^{L/2} P_n(2z'/L) \frac{(e^{-jk|\mathbf{r}-\mathbf{r'}|} - 1)}{|\mathbf{r}-\mathbf{r'}|} \, dz' \, d\varphi. \qquad (6\text{--}3)$$

The superscripts s and f designate the static and frequency-dependent part of the potential integral. The electrostatic potential integral, $\kappa_{s\,n}^s$, is discussed in part A. The integration of the nonsingular kernel of the potential integral, $\kappa_{s\,n}^f$, is discussed in part B.

PART A: STATIC POTENTIAL INTEGRAL

The evaluation of the potential integral can be simplified by looking at the kernel of equation (6–1). The value of the potential integral depends on the distance, $|\mathbf{r}-\mathbf{r'}|$, from the field point to a point on the segment. In most cases, this distance from the segment to the field point is large compared to the radius of the wire. The integration along the length of the segment is an excellent approximation of the potential integral, κ_n; the angular integration is a small correction to the potential integral. For this reason, we integrate over the length of the segment first, then use a Gauss-Chebyshev integration formula to integrate around the circumference of the segment. A sequence of Gauss-Chebyshev integration formulas is used to compute the angular integration. Close to the surface of the segment, the kernal can be modified to improve the convergence. The angular integration can be performed to any desired accuracy.

Butler (1975) analytically integrated the singular term in the kernel. The angular integration was expanded in power series and integrated term by term. For the general

43

Legendre-polynomial charge distribution, the power series is too complicated to be of use. The nonsingular kernel can be easily integrated with a sequence of Gauss-Chebyshev integration formulas.

This numerical method is illustrated for the simple case n = 0. The general results are given in appendix A. The integration along the surface of the cylinder yields

$$\kappa_0^S(\rho,z) = \frac{1}{2\pi}\int_0^{2\pi} \ln\left[\frac{1+\tau}{1-\tau}\right]d\varphi', \tag{6-4}$$

where $\quad \tau = \dfrac{L}{R_1+R_2},$

$$R_1 = \sqrt{(z+L/2)^2+\rho^2-2a\rho\cos\varphi'+a^2},$$

and

$$R_2 = \sqrt{(z-L/2)^2+\rho^2-2a\rho\cos\varphi'+a^2}.$$

The variable, R_1, is the distance from the bottom edge (a, φ', $-L/2$) of the cylinder to the field point. The variable, R_2, is the distance from the top edge (a, φ', $L/2$) of the cylinder to the field point. The argument of the natural logarithm in equation (6–4) can be calculated very accurately by using one of several different algebraically equivalent forms, equations (A–13), (A–14), and (A–15) in appendix A. The potential near the surface of the wire, equation (A–15), can be simplified to improve the numerical convergence. The term $\ln(\rho^2-2a\rho\cos\varphi'+a^2)$ in equation (A–15) is the potential of an infinite line charge at φ' and $\rho = a$. The angular integral of $\ln(\rho^2-2a\rho\cos\varphi'+a^2)$ gives the potential for an infinite cylinder $\ln(\rho^2)$ for $\rho > a$ and $\ln(a^2)$ for $\rho \le a$. The details are given in appendix A.

The singular part of equation (6–4) can be integrated to give exact results, equations (6–5a) and (6–5b). *Equations (6–5a) and (6–5b) are not approximations.*

$$\kappa_0^S(\rho,z) = \frac{1}{2\pi} \int_0^{2\pi} \ln\left[\frac{(z+L/2+R_1)(R_2-z+L/2)}{\rho^2}\right] d\varphi' \quad \text{for } \rho > a \text{ and } |z| < L/2,$$

$$(6\text{--}5a)$$

$$\kappa_0^S(\rho,z) = \frac{1}{2\pi} \int_0^{2\pi} \ln\left[\frac{(z+L/2+R_1)(R_2-z+L/2)}{a^2}\right] d\varphi' \quad \text{for } \rho \leq a \text{ and } |z| < L/2$$

$$(6\text{--}5b)$$

The potential at the end of the segment $|z| = L/2$ is discussed in appendix A.

The integral around the cylinder can be simplified by making the substitution $\cos\varphi' = x$.

$$\kappa_0^S(\rho,z) = \frac{1}{\pi} \int_{-1}^{1} \ln\left[\frac{1+\tau(x)}{1-\tau(x)}\right] \frac{dx}{\sqrt{1-x^2}} . \qquad (6\text{--}6)$$

This integral can be evaluated by using the Gauss-Chebyshev integration formula. The Chebyshev polynomials are

$$T_N(x) = \cos(N \cos^{-1}(x)),$$

where $-1 \leq x \leq 1$. The quadrature points are the roots of $T_N(x)$:

$$N \cos^{-1}(x_i) = \frac{\pi}{2} + i\pi \quad \text{for } 0 \leq i \leq N-1$$

or

$$x_i = \cos[\pi(i+1/2)/N].$$

In the Gauss-Chebyshev integration formula each quadrature point has a weight

$$w_i = \pi/N.$$

The Gauss-Chebyshev integration formula for our integral is

$$\int_{-1}^{1} f(x) \frac{dx}{\sqrt{1-x^2}} = \sum_{i=0}^{N-1} w_i f(x_i).$$

The constant $1/\pi$ in equation (6–6) can be expressed in terms of the total charge on the wire, $Q = L$.

$$\kappa_0^s(\rho,z) = \frac{Q}{LN} \sum_{i=0}^{N-1} \ln\left[\frac{1 + \tau(x_i)}{1 - \tau(x_i)}\right]. \tag{6–7}$$

The angular integration in equation (6–7) has a simple interpretation. The constant surface charge density is approximated with 2N line-charge distributions with a constant charge per unit length. The total charge on each line is $Q/(2N)$. The line charge distributions are located at $\varphi_i' = \pi(i+1/2)/N$ and $\rho' = a$; the symmetry in the angular distribution allows the number of terms in the sum to be reduced to N. Equation (6–7) is equivalent to

$$\kappa_n(\rho,z) = \int_{-L/2}^{L/2} \frac{Q}{LN} \sum_{i=0}^{N-1} \frac{1}{[(z-z')^2+\rho^2+a^2-2a\rho\cos\varphi_i]^{1/2}} dz. \tag{6–8}$$

When $N = 1$, equation (6–8) is the reduced kernel approximation. In the reduced kernel approximation, $|r-r'|$ is replaced by $[(z-z')^2+\rho^2+a^2]$. *Equation (6–8) is a generali-*

zation of the reduced kernel approximation. The angular integration of the potential integral is the same for the general-charge distributions, $P_n(2z'/L)$.

The error in the angular integration can be calculated by using the symmetry of the 2N line charges and a spherical harmonic expansion (Jackson, 1975) of $\kappa_n^S(\rho,z)$. The spherical harmonic expansion is

$$\kappa_n^S(r,\theta,\phi) = \sum_{l=0}^{\infty} \sum_{m=-l}^{l} B_{lm} r^{-(l+1)} Y_{lm}(\theta,\phi), \qquad (6\text{--}9)$$

which is valid in a charge-free region, $r > ((L/2)^2 + a^2)^{1/2}$. The variables r, θ, and ϕ define a spherical coordinate system; r is the distance from the origin, θ is the angle from the z-axis, and ϕ is the angle measured around the z-axis ($\phi = 0$ in x–z plain). The $m = 0$ terms are cylindrically symmetric. The $m \neq 0$ terms have an m–fold rotational symmetry and vanish on the z-axis.

The rotational symmetry of the kernel ensures that *all the Gauss-Chebyshev integration formulas are exact on the z-axis.* The potential integral, $\kappa_{s\,n}^S$ on the z-axis, uniquely determines the value of all the cylindrically symmetric terms; they are the same for all Gauss-Chebyshev integration formulas. The nonsymmetric terms represent the error in the Gauss-Chebyshev integration formulas.

The 2N line-charge distributions and the spherical harmonic expansion must have the same rotation symmetry. The 2N line-charge distributions, $P_n(2z'/L)$, are symmetric under rotations of $2\pi/2N$ radians. Consequently, the leading error term has $m = 2N$, where $l \geq m$. The value of l depends on the symmetry of the charge distribution on the segment. The charge distribution $P_n(\theta)$ is even for even n; the potential, $Y_{lm}(\theta,\phi)$, is even if l is even and $l \geq 2N$. The charge distribution, $P_n(\theta)$, is odd for odd n; the potential, $Y_{lm}(\theta,\phi)$, is odd if l is odd and $l \geq 2N+1$. The radial dependence of the first error term is

$r^{-(2N+1)}$ for even n and $r^{-(2N+2)}$ for odd n. The accuracy of the angular integration increases quickly with the order N of the Chebyshev quadrature formula.

This error analysis must be modified if $r < ((L/2)^2 + a^2)^{1/2}$. In this case, the potential is expanded using modified Bessel functions (Jackson, 1975). In a cylindrical coordinate system:

$$\kappa_n^S(\rho,\phi,z) = \int_0^\infty \sum_{\nu=0}^\infty (A_\nu(k)\cos(kz) + B_\nu(k)\sin(kz))K_\nu(k\rho)e^{-j\nu\phi}dk.$$

(6–10)

This expression is valid for $\rho > a$. The variable k is a continuous parameter; k is not the wave number. The $\nu = 0$ terms are cylindrically symmetric. The error term has a 2N rotational symmetry, $\nu = 2N, 4N, 6N$, etc. In this case, the error is a continuous function of k. The radial dependence is determined by the $K_\nu(k\rho)$ factor. The factor, $K_\nu(k\rho)$, has the limits:

$$K_\nu(k\rho) = \frac{\Gamma(\nu)}{2}\left[\frac{2}{k\rho}\right]^\nu \quad \text{for } \nu \neq 0 \text{ and } k\rho << 1,$$

(6–11a)

$$K_\nu(k\rho) = \left[\frac{\pi}{2k\rho}\right]^{1/2}e^{-k\rho}\left[1 + O\left[\frac{1}{k\rho}\right]\right] \quad \text{for } k\rho >> 1.$$

(6–11b)

Equation (6–11a) applies near the surface, $\rho \simeq a$ and $k << 1/a$. Equation (6–11b) applies at larger distances, $\rho \simeq L/2$, where $k >> 2/L$. For most values of k, the error terms fall off as ρ^{-2N} near the surface of the wire.

The angular integration can be computed with a sequence of Chebyshev quadrature formulas with N = 1, 3, 9, 27, 81. This sequence requires the minimum number of new

quadrature points[4] for each new iteration. The error in the iterations $N = 1, 3, 9, 27, 81$ falls off as $1/r$ (or $1/\rho$) to the power 3, 7, 19, 55, 163, respectively. The power of the r more than doubles for the second and third iteration; it almost triples for the fourth and fifth iteration.

The error in each integration can be estimated by using the previous iteration. The normalized error$_p$ in the p iteration of the static potential integral, $\kappa_n^S(r,\theta,0)_p$, is

$$\kappa_n^S(r,\theta,0)_{\text{exact}} = \kappa_n^S(r,\theta,0)_p\left[1 + \text{error}_p\right], \tag{6-12}$$

where $\kappa_n^S(r,\theta,0)_{\text{exact}}$ is the exact-potential integral. The error in the sequence of iterations obeys the relationship:

$$\text{error}_{p+1} < \text{error}_p^2. \tag{6-13}$$

The normalized iteration difference (NID) is

$$\text{NID}_n(p{-}1,p) = \left|\frac{\kappa_n^S(r,\theta,0)_{p-1} - \kappa_n^S(r,\theta,0)_p}{\kappa_n^S(r,\theta,0)_p}\right|. \tag{6-14}$$

The NID can be expressed in term of the error$_{p-1}$

$$\text{NID}_n(p{-}1,p) \simeq \text{error}_{p-1} - \text{error}_p. \tag{6-15}$$

The second term, error$_p$, in the above equation is much smaller than the first term; it can

---

4. L. Koyama pointed out that the Gauss-Chebyshev integration formulas have some common evaluation points.

49

be neglected. The error in the pth iteration is less than $error_{p-1}^2$. In terms of the NID(p–1,p), the $error_p$ is

$$error_p < NID(p–1,p)_n^2. \tag{6–16}$$

The error in the present iteration is the less than square of the difference between the present and previous iterations. The iteration sequence can be stopped when the NID is 10^{-8} for double precision and 10^{-4} for single precision.

The above conclusions are verified with a computer calculation of the static potential integral at a distance, L, from the center of a segment with a length, L, and radius, 1/2. The NID for n = 0 and 1 was calculated for the range $0 \le \theta \le \pi/2$; the largest value for this range is given in table 6–1. For n > 1, the NID is normalized with the potential on the z-axis is

$$NID_n(p–1,p) \simeq \left| \frac{\kappa_n^S(L,\theta,0)_{p-1} - \kappa_n^S(L,\theta,0)_p}{\kappa_n^S(L,0,0)_p} \right| \text{ for n > 1.} \tag{6–17}$$

The largest NID for n > 1 is given in table 6–1. The NID in the second row is less than the square of NID in the first rows. The NID in the third row is limited by the precision of the computer.

In section 5, we discussed the functional form of the potential at large distances from the segment. This algorithm allows the static potential integral, $\kappa_{s\,n}^S$, to be computed near the surface of a wire. Figure 6–2a plots the static potential integral, $\kappa_{s\,n}^S$, along the surface of the source segment and the nearest-neighbor segments. The source segment is centered at x = 0, with a length of 10 and a radius of 1/2. Figure 6–2b uses an expanded scale for the static potential integrals, $\kappa_{s\,n}^S$, on the surface of the next two segments. This plot shows that the multipole static potential integrals, $\kappa_{s\,n}$, falls off very fast.
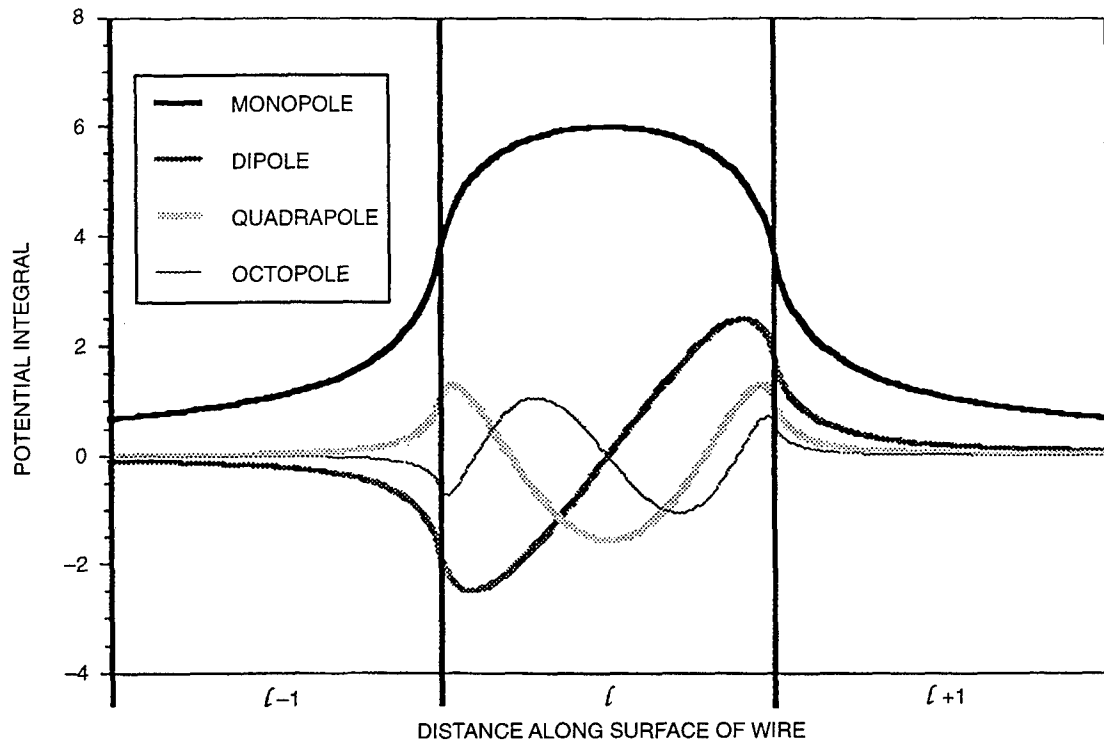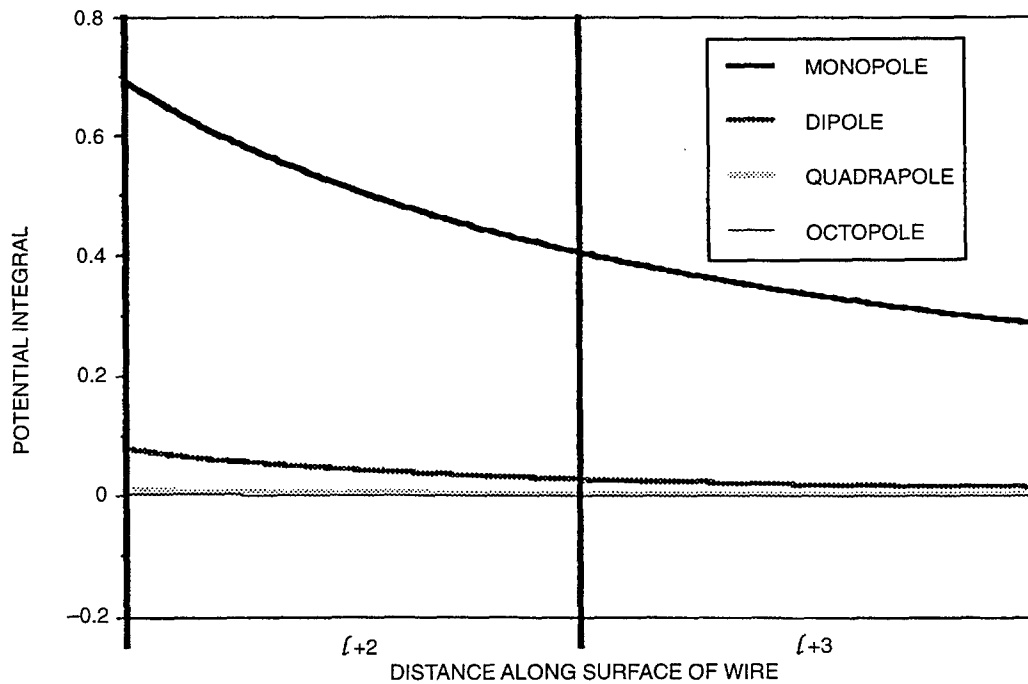
Figure 6-2. Potential integral on the surface of a wire produced by a source on segment ℓ, where (a) is the potential near source and (b) is the potential on the second and third segments (length, L=100, and radius, a=1/2).

51

Table 6–1. Normalized iteration difference in the angular integration on a spherical shell with the radius of 10 for (a) and 100 for (b).

Iteration Difference	Monopole	Dipole	Quadrupole	Octupole
1–2	2×10^{-3}	3×10^{-3}	3×10^{-3}	4×10^{-3}
2–3	7×10^{-9}	3×10^{-8}	8×10^{-8}	2×10^{-7}
3–4	5×10^{-16}	5×10^{-12}	3×10^{-12}	6×10^{-12}

(a) Segment length is 10 and radius is 1/2.

Iteration Difference	Monopole	Dipole	Quadrupole	Octupole
1–2	2×10^{-5}	4×10^{-5}	6×10^{-5}	1×10^{-4}
2–3	7×10^{-15}	2×10^{-11}	8×10^{-14}	2×10^{-13}
3–4	5×10^{-15}	5×10^{-15}	3×10^{-16}	6×10^{-17}

(b) Segment length is 100 and radius is 1/2.

Figures 6–3a and 6–3b show the potentials for a higher aspect-ratio segment with a length of 100 and radius of 1/2. The aspect ratio is the segment length divided by the segment radius. Figure 6–3a shows the static potential integral, $\kappa^s_{s\,n}$, for the source segment and the two adjacent segments. Figure 6–3b shows the static potential integral, $\kappa^s_{s\,n}$, of the next two segments. The plots show that the high-order static-potential integral, $\kappa^s_{s\,n}$, is large only on segments near the source segment.

The static potential integral, $\kappa^s_{s\,n}$, for the two different aspect-ratio segments have the same shape as the Legendre polynomial charge distribution. Therefore, the potentials

52
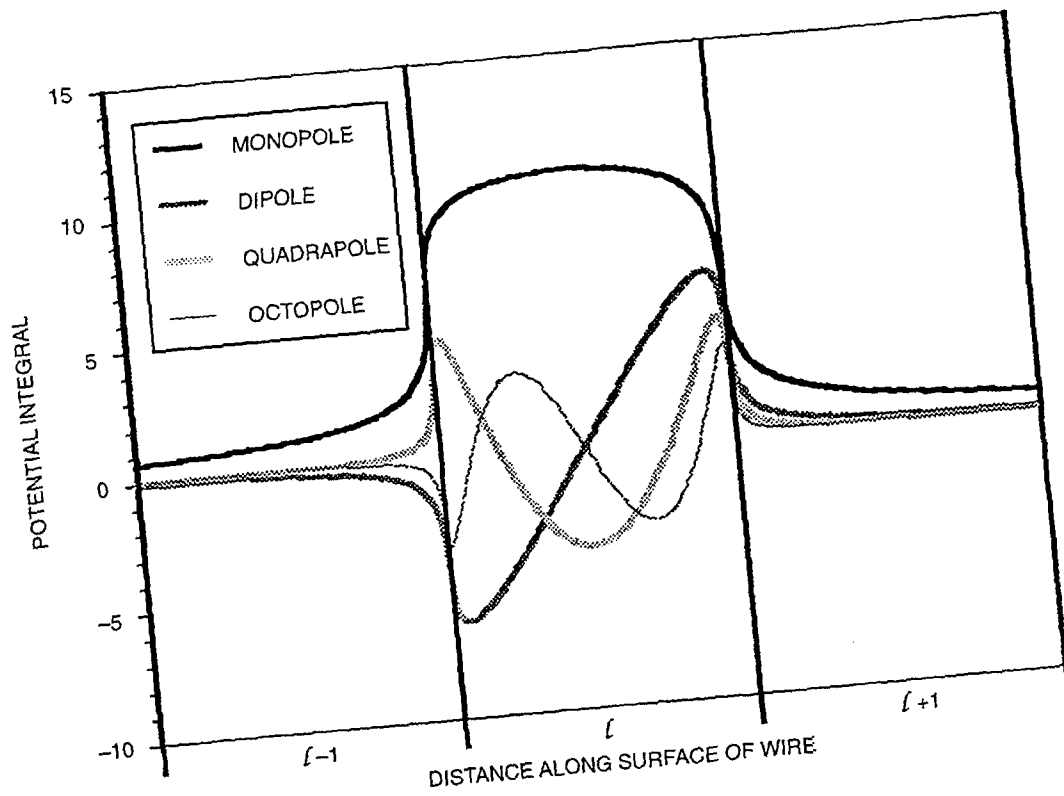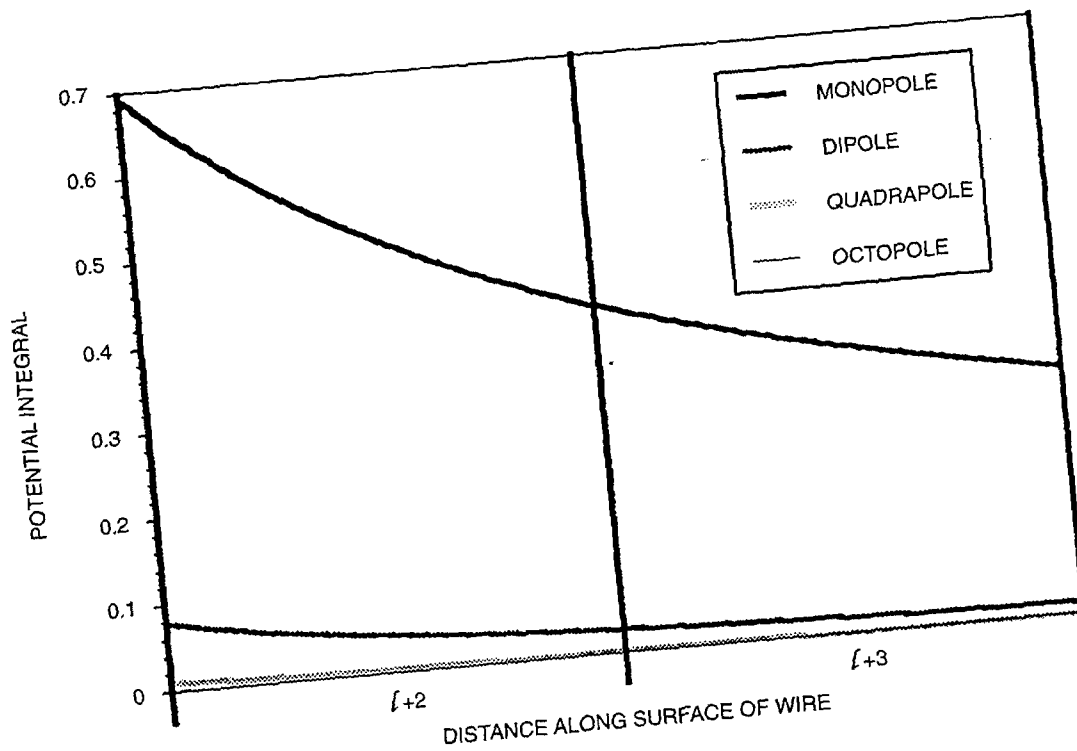
Figure 6-3. Potential integral on the surface of a wire produced by a source on segment ℓ, where (a) is the potential near source and (b) is the potential on the second and third segments (length, L=100, and radius, a=1/2).

53

should have the same values at the end of the segment where $P_n(1) = 1$. The static potential integrals, $\kappa^S_{s\,n}$, for the high aspect-ratio segment are nearly the same at the end of the segment. For the short segment, the difference in the static potential integrals, $\kappa^S_{s\,n}$, is large at the end of the segment. In addition, the slope of the potentials at the end of the segment is much higher for the high aspect-ratio wire. The shape of the potentials at the end of the wire is determined by the details of the local charge distribution at the end of the segment.

The charge distribution on the short segment changes very fast compared to the wire radius. Any details in the charge distribution smaller than a wire radius are averaged out by the potential integral. For high aspect-ratio segments, the charge distribution changes very slowly. For high aspect-ratio segments, the values of the potential integral will be almost the same near the end of the segment ($t_s = 1$). The sharp falloff in the potential at the end of the segment is caused by discontinuity in the charge distribution at the end of the segment. The sharp drop is limited to a distance of about six wire radii. This sharp drop in the potential can affect the accuracy of the boundary-condition calculation. Details smaller than a wire radius cannot be resolved by this approach.

The shape of the vector potential integral, $\kappa^S_{s\,n+1} - \kappa^S_{s\,n-1}$, also depends on the shape of the current basis functions. In contrast to the charge basis functions, the current basis function is zero at the end of each segment. This eliminates the sharp falloff in the shape of the vector potential integral, $\kappa^S_{s\,n+1} - \kappa^S_{s\,n-1}$. Figures 6–4 and 6–5 show the shape of the vector potential integral, $\kappa^S_{s\,n+1} - \kappa^S_{s\,n-1}$, for second and third current basis function. Figure 6–4 is for a segment with a length of 10 and a radius of 1/2. Figure 6–5 is for a longer segment with a length of L = 100 and a radius of 1/2.

The plot shows that the higher multipole basis functions contribute very little to the scalar potential integral, $\kappa^S_{s\,n}$, on nonadjacent segments. The falloff in the potential integral, $\kappa^S_{s\,n}$, determines the magnitude of the off-diagonal terms in the impedance matrix.

54
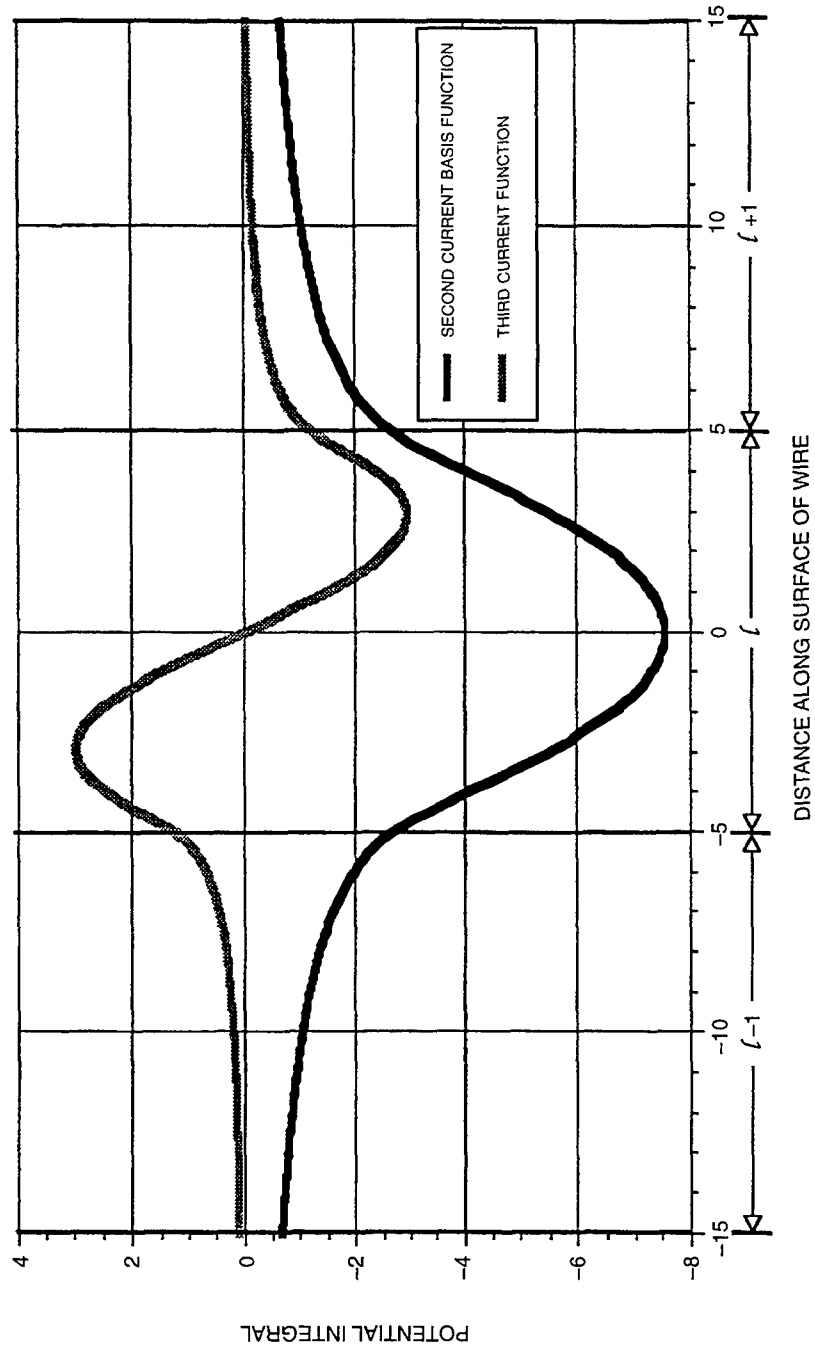
Figure 6-4. Vector potential on surface of wire (length, L=10, and radius, a=1/2).
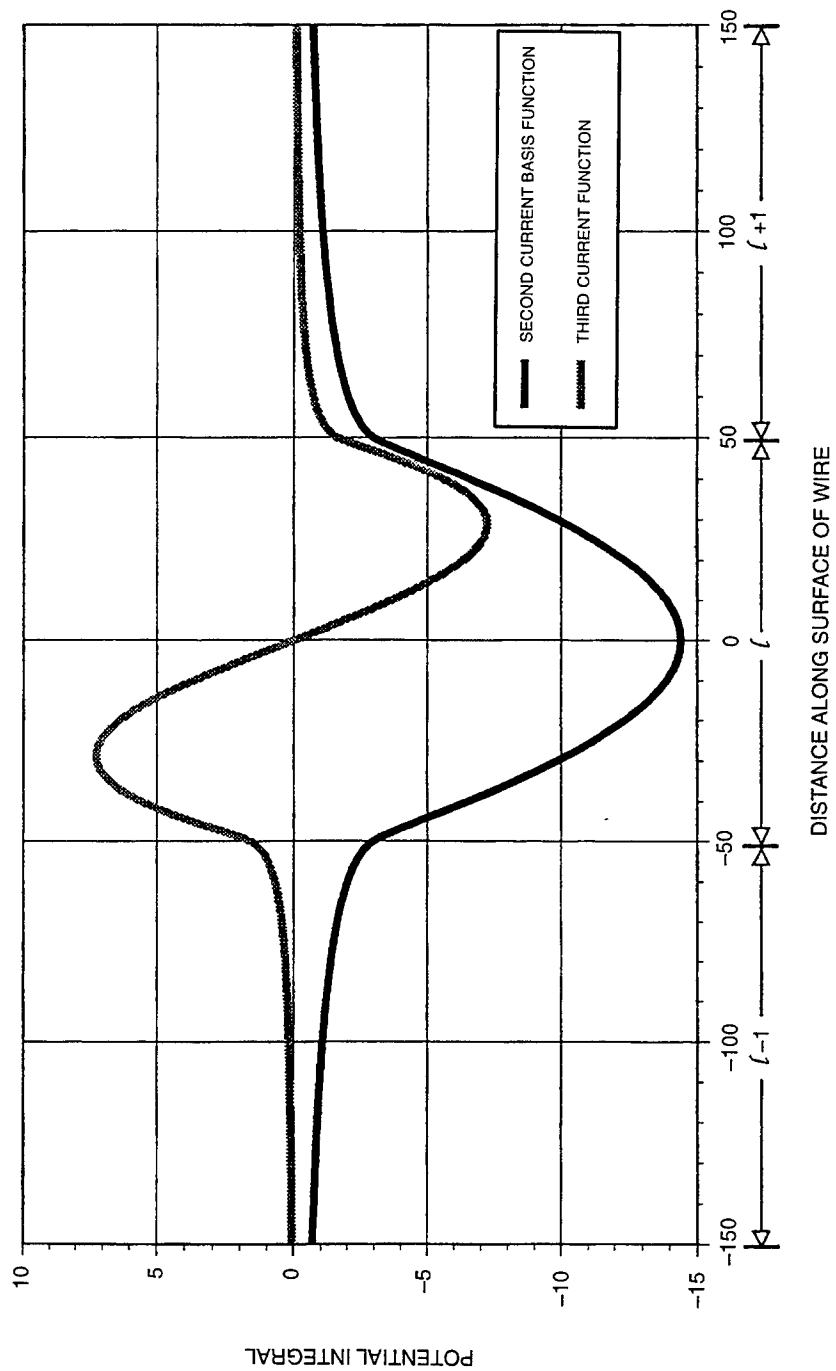
Figure 6-5. Vector potential on surface of wire (length, L=100, and radius, a=1/2).

56

A detailed discussion of the individual terms and error in the impedance matrix is given in section 8.

PART B: FREQUENCY-DEPENDENT POTENTIAL INTEGRAL

The frequency part of the kernel can be numerically integrated with the same technique used in part A. In this case, the integral of each line-charge distribution is evaluated by Gauss-Legendre integration. The annular integral will be integrated by using the same sequence of Gauss-Chebyshev integration formulas. The number of Gauss-Legendre quadrature points needed in the integration of the line-charge distributions depends on the number of segments per wavelength. In this report, we will assume two or more segments per wavelength. The error analysis used in part A does not apply to the integration of this part of the kernel.

The integration of the frequency-dependent part of Green's function gives a complex result. The real and imaginary part of the integral are considered separately. The imaginary part has the form:

$$Im\kappa_n^f(r) = -k\frac{Q}{LN}\sum_{i=0}^{N-1}\int_{-L/2}^{L/2} P_n(2z'/L)\sin(k|r-r'|)/(k|r-r'|)dz'.$$

(6–18)

The integrand and its derivatives are continuous for all $|r-r'|$. This integral can be accurately evaluated with a Gauss-Legendre integration formula.

For electrically small antennas, the integral will have large numerical errors for the high-order basis functions. An error in the evaluation of this integral will introduce an

error in the feed point resistance of an electrically small antenna. Equation (6–18) can be optimized for low frequencies by using an alternative form:

$$\mathrm{Im}\kappa_n^f(r) = \frac{kQ}{LN} \sum_{i=0}^{N-1} \left[-L\delta_n^0 + \int_{-L/2}^{L/2} P_n(2z'/L)\left[1 - \frac{\sin(k|r-r'|)}{(k|r-r'|)}\right]dz' \right].$$

(6–19)

The constant terms, $L\delta_n^0$, cancel for the two square-charge pulses created by the triangular current basis function. This cancellation would give a large roundoff error for electrically small antennas. The impedance matrix is computed with the right side of equation (6–19). The constant term, $L\delta_n^0$, is computed as a separate term; the $L\delta_n^0$ term is added to the potentials used to compute the $J_{s\,0}$ and $J_{s\,1}$ terms in the impedance matrix. The difference between the kernel and unity must be computed with an infinite series to achieve the desired accuracy.

The real part of the frequency potential integral, $\kappa_{s\,n}^f$, has the form:

$$\mathrm{Re}\kappa_n^f(r) = -\frac{Q}{LN} \sum_{i=0}^{N-1} \int_{-L/2}^{L/2} P_n(2z'/L)\sin^2\left[\frac{k|r-r'|}{2}\right] /(|r-r'|)dz'.$$

(6–20)

The integrand is continuous, but its derivative does not exist at $|r-r'| = 0$. The integration of equation (6–20) is simple for large $|r-r'| > L$. For small $|r-r'| < L$, the integration interval is divided into two smooth parts. The dividing line is the point where $|r-r'|$ is minimum. On the source segment, a 7-place accuracy can be achieved by using a 42-point Gauss-Legendre integration formula for each interval. On the other segment, a 14-place accuracy can be achieved with 42-point Gauss-Legendre integration formula.

7 BOUNDARY CONDITION

The boundary condition for a perfect conductor requires the electric field to be perpendicular to the surface of the conductor. Therefore, the parallel component of the electric field, $E_\parallel$, must vanish on the surface of the conductor. For thin-wire antennas, the boundary condition is only imposed on the electric fields parallel to the length of the wire. No boundary condition is imposed upon the electric fields perpendicular to the length of the wire. This approximation introduces an error in the angular charge distribution on the wire. Our discussion is limited to antennas excited at a single feed point.

In the method of moments, the boundary condition is an approximation of the ideal boundary condition. The approximation of the ideal boundary condition introduces a modeling error in the boundary condition. The boundary condition is calculated from the scalar and vector potentials. The scalar and vector potentials are implicitly a function of all the charge and current distributions on all the segments. The modeling error in the charge distribution will induce an error in the boundary condition. Likewise, the modeling error in the boundary condition also induces an error in the charge distribution. In addition, the numerical evaluation of the boundary conditions will introduce errors in the boundary condition. The interaction of these errors on the single segment is discussed in this section. The general discussion is given in the next section.

The boundary condition developed in this section is a generalization of the pulse-testing boundary condition. The pulse-testing boundary condition integrates the product of $E_\parallel$ and a testing function. The boundary condition is imposed by requiring the tested electric field to vanish. The testing function, $w(s)$, is typically a triangular or square-testing function. In this report, we only consider square-testing functions. The square-testing function, $w(z(t_f))$, is 1 between the points $z(t_1)$ and $z(t_2)$; it vanishes for all other points:

$$\langle w, E_\parallel \rangle = \int_{z(t_1)}^{z(t_2)} w(z)\, E(z) \cdot dz. \qquad (7\text{--}1)$$

The boundary condition is

$$\langle w, E_\parallel \rangle = 0.$$

In our case, N square-testing functions for each segment are required for the N charge basis functions.

For square-testing functions, the right side of equation (7–1) is the integral of $E_\parallel$ between the points $z(t_1)$ and $z(t_2)$. This integral is the electromotive force (EMF) between the points t_1 and t_2. The $EMF(t_1, t_2)$ is the energy gained by moving a unit charge from point t_1 to point t_2 on the surface of the wire. Ideally, the energy gained by moving a unit charge on the surface should be zero at all points. The EMF can be expressed in terms of the potentials:

$$EMF(t_1, t_2) = \phi(t_1) - \phi(t_2) - j\omega \int_{z(t_1)}^{z(t_2)} A(z) \cdot dz. \qquad (7\text{--}2)$$

The width of the testing function does not need to be the same for each testing function. Michalski and Butler (1983) used variable-width testing functions to analyze scattering from a finite-length cylinder. The boundary condition for N basis functions could be imposed by using N testing functions for each segment. The functional form of the boundary condition error on each segment is controlled by the width of the N testing pulses. However, the magnitude of the numerical error on the segment is unknown. The functional

form and the magnitude of the error can be derived by interpreting the boundary-condition equations in a different way.

Instead of looking at the EMF for individual testing pulse, the EMF should be interpreted as a continuous function on the entire antenna being modeled. The $\mathrm{EMF}(t_f)$ on the segment is the line integral from the center of the feed point to the point t_f on the segment f:

$$\mathrm{EMF}(t_f) = \int_0^{z(t_f)} E(z)\cdot dz = \phi(0) - \phi(t_f) - j\omega \int_0^{z(t_f)} A(z)\cdot dz. \tag{7-3}$$

The integration of the vector potential is a line integral along the surface of the antenna wires. Ideally, the $\mathrm{EMF}(t_f)$ on the antenna should be a constant equal to half of the input voltage.

The $\mathrm{EMF}(t_f)$ function on a segment is approximate by a sum of Legendre polynomials.

$$\mathrm{EMF}(t_f) = \sum_{k=0}^{N-1} \alpha_{fk} P_k(t_f). \tag{7-4}$$

The N boundary conditions for each segment are imposed by setting the expansion constants equal to

$$\alpha_{f0} = \tfrac{1}{2}V_{in}$$

$$\alpha_{fk} = 0 \quad \text{for } 0 < k < N. \tag{7-5}$$

The first error term in this boundary condition is $P_N(s)$.

The expansion coefficient, α_{fk}, is evaluated by computing the integral

$$\alpha_{fk} = (k+\tfrac{1}{2}) \int_{-1}^{1} P_k(t_f) \text{EMF}(t_f) dt_f. \tag{7-6}$$

This integral can be evaluated *very accurately* with an M-term Gauss-Legendre integration formula, where $M \geq N$:

$$\alpha_{fk} = \sum_{i=0}^{M-1} \beta_{ki} \text{EMF}(t_{if}), \tag{7-7}$$

where

$$\beta_{ki} = (k+\tfrac{1}{2}) w_i P_k(t_{if}).$$

The points t_i are the quadrature points and w_i are the quadrature weights. If $M > N$, equation (7-7) gives extra expansion coefficients. These extra expansion coefficients, α_{fN} to α_{fM-1}, represent the modeling error in the boundary condition.

The boundary-condition error is caused by using a finite number of basis functions to model the charge distribution. The charge distribution on each segment is modeled by the charge basis functions, $P_0(t_f)$ through $P_{N-1}(t_f)$. The first error term in the charge distribution is $P_N(t_f)$. The $P_N(t_f)$ charge basis function contributes an error, $\kappa_N(t_f)$, to the scalar potential in the boundary condition. The $\kappa_N(t_f)$ error has the same shape as $P_N(t_f)$ on the source segment. The high-order charge basis functions, $P_N(t_f)$, $P_{N+1}(t_f)$, etc., to first approximation will cause errors, $P_N(t_f)$, $P_{N+1}(t_f)$, etc., in the boundary condition. These errors could affect the numerical evaluation of the boundary condition.

The numerical evaluation of the integral introduces some error in the boundary condition. The M-point Gauss-Legendre integration formula is exact for polynomials with

a degree less than 2M. Thus, the first error term[5] in the evaluation of the expansion coefficient, α_0, is caused by t^{2M} or $P_M^2(t_f)$ errors in the EMF(t_f) function. *The modeling error terms $P_N(t_f)$ to $P_{2M-1}(t_f)$ in the EMF(t_f) function have no impact on the numerical calculation of the coefficient α_0.* As a consequence, the error in the far field is very small. In general, the expansion coefficient, α_k, is exact for polynomials with a degree less than 2M−k. The error in the expansion coefficient, α_k, is larger; however, this error is a high-order multipole moment. The high-order multipole moments are large only in the near fields. The error terms in the numerical boundary condition, α_N through α_{M-1}, are a good estimate of the error in the boundary condition.

The above summary of the error analysis assumes that the potential integral is a smooth function that can be modeled with low-degree polynomials. This is true for the interior of the segment; however, it is not true at the end of the segment. The distance from the peak in potential integral $\kappa_{s\,1}$ to the end of the segment is 6.7 wire radius. This sharp drop would introduce a large error in the evaluation of the expansion coefficient, α_{fk}. The Gauss-Legendre integration with M = 4 requires a segment with an aspect ratio larger than 85. Table 7–1 gives the minimum aspect ratio for different order Gauss-Legendre integration formulas. The minimum aspect ratios given in table 7–1 avoid the sharp drop near the end of the segment; the first Gauss-Legendre point is a distance of 6 wire radius from the end of the segment. The aspect ratio of the segment limits the number basis allowed on each segment.

The end effect could cause an error in the electric-field boundary condition at the junction of two segments. However, if the charge distribution is continuous, the end effects

---

5. The general form for the error term in the integrand of the M-point quadrature formula is $s^n P_M(s)$. This error term is zero at the quadrature points. The factor s^n can be expressed as the sum of $P_0(s)$ to $P_N(s)$. The first term to have a non-zero integral is $P_M^2(s)$; therefore, the first error term in the integral has the power s^{2M}.

Table 7–1. Minimum aspect ratio.

Order Gauss-Legendre Integration	Aspect Ratio
4	85
5	130
6	180
7	240
8	300
9	375

cancel out. At the free end of a wire, the end effect will cause an error in the boundary condition; this error is limited to a 6 radius distance, In addition, at the free end of a wire, several high-order polynomials are required to model the charge distribution. These high-order polynomials may introduce errors in the evaluation of the boundary condition. The numerical results in section 2 show that the boundary condition is very stable at the end of the wire.

This boundary condition is simple in antennas without closed loops. In a loop, the point t_f can be reached by using two different integration paths. The $EMF(t_f)$ needs to be independent of the integration path. The scalar part of the EMF is independent of the integration path; however, the integral of the A vector depends on the integration path. The integral of the A vector on a closed loop is evaluated with Stokes' theorem,

$$\oint A(z) \cdot dz = \phi, \tag{7–8}$$

where ϕ is the total magnetic flux passing through the loop. In a closed perfect conducting

loop, the magnetic flux through the loop is zero. The EMF boundary condition requires the total magnetic flux through each loop to vanish.

The above arguments indicate that the coefficients, α_n, are determined very accurately for a smooth charge distribution. Near the end of a wire, the error should be a high-order multipole moment. The magnitude of the error in the EMF boundary condition is easily calculated.

8 IMPEDANCE MATRIX

In this section, the basis functions and boundary condition are used to construct the impedance matrix for the method of moments. The boundary-condition errors can be estimated by computing extra terms in the impedance matrix. The errors and approximations used in constructing the impedance matrix are discussed in detail. For the dipole problem, the rows and columns can be arranged to eliminate the need for pivoting in the solution of the impedance matrix. The Legendre-polynomial basis functions are compared to the power series basis functions used by Djordjevic et al., (1990). A matrix transformation is developed to compare the EMF boundary conditions to the pulse-testing boundary conditions. The EMF boundary condition produces a matrix with smaller off-diagonal terms.

The impedance matrix relates the mth boundary condition expansion coefficient α_{fm} on segments f to the nth basis function coefficient $\chi_{s\,n}$ on segments s:

$$\alpha_{fm} = \sum_{s} \sum_{n} Z_{fs\,mn} \chi_{s\,n}. \tag{8-1}$$

For $n > 0$, $\chi_{s\,n}$ is the coefficient, $\eta_{s\,n}$, for the charge basis functions on each segment s. For $n = 0$, $\chi_{s\,0}$ is the coefficient, $\delta_{s\,0}$, of the current basis function. Note, the free end of the wire does not require a current basis function.

Equation (8-1) can be expressed in matrix form:

$$
\begin{bmatrix}
\alpha_{f0} \\
\alpha_{f1} \\
\alpha_{f2} \\
\cdot \\
\alpha_{fp} \\
\cdot \\
\alpha_{fm}
\end{bmatrix}
=
\begin{bmatrix}
Z_{fs\,00} & Z_{fs\,01} & Z_{fs\,02} & \cdot & Z_{fs\,0k} & \cdot & Z_{fs\,0n} \\
Z_{fs\,10} & Z_{fs\,11} & Z_{fs\,12} & \cdot & Z_{fs\,1k} & \cdot & Z_{fs\,1n} \\
Z_{fs\,20} & Z_{fs\,21} & Z_{fs\,22} & \cdot & Z_{fs\,2k} & \cdot & Z_{fs\,2n} \\
\cdot & \cdot & \cdot & \cdot\,\cdot & \cdot & & \cdot \\
Z_{fs\,p0} & Z_{fs\,p1} & Z_{fs\,p2} & & Z_{fs\,pk} & & Z_{fs\,pn} \\
\cdot & \cdot & \cdot & & & & \\
Z_{fs\,m0} & Z_{fs\,m1} & Z_{fs\,m2} & \cdot & Z_{fs\,mk} & \cdot & Z_{fs\,mn}
\end{bmatrix}
\begin{bmatrix}
\delta_{s0} \\
\eta_{s1} \\
\eta_{s2} \\
\cdot \\
\eta_{sk} \\
\cdot \\
\eta_{sn}
\end{bmatrix}
$$

$$(8\text{--}2)$$

The element, $Z_{fs\,pk}$, represents submatrix and the elements α_{fp}, δ_{sk}, and n_{sk} subcolumns of the matrix equation (8–1). The submatrix, $Z_{fs\,pk}$, represents the interaction between all the segments f and s in the antenna for a fixed basis function, k, and a fixed boundary condition expansion coefficient, p. The subcolumn, α_{fp}, represents a fixed boundary condition expansion coefficient, p, for all the segments, f, in the antenna. The subcolumn, δ_{s0}, is the coefficient of the triangular current basis function for all the segments, s, in the antenna. The subcolumn, η_{sk}, represents the coefficient for a fixed charge basis function, P_k (k $\neq$ 0), for all the segments, s, in the antenna. The reason for this structure will be discussed later. The boundary condition is imposed by setting the coefficients, $\alpha_{f0} = 1/2$ and $\alpha_{fm} = 0$ (m $\neq$ 0), for each segment f.

The impedance matrix, $Z_{fs\,mn}$, depends on the $\text{EMF}(t_f)$ at the point t_f on segment f. The $\text{EMF}(t_f)$ is a function of the EMF caused by all the current and charge distributions on all segments, s, in the antenna:

$$
\text{EMF}(t_f) = \sum_{n=0}^{N-1} \sum_{s=1}^{R} \text{EMF}_{s\,n}(t_f) + \sum_{n=0}^{N-1} \sum_{s=-1}^{-R} \text{EMF}_{s\,n}(t_f).
\qquad (8\text{--}3)
$$

The first term represents the EMF of one arm of the dipole. The second term is the symmetric image term. The following calculations are for the first term in equation (8–3). The image is computed with the same method. Note, the triangular pulse at the source is

split between the first and second terms. The right side is labeled δ_1 and the left side is labeled δ_{-1}.

The $\text{EMF}_{s\,\text{n}}(t_f)$ on segment f caused by the nth basis function on segment s is

$$\text{EMF}_{s\,\text{n}}(t_f) = \phi_{s\,\text{n}}(0) - \phi_{s\,\text{n}}(t_f) - j\omega \int_0^{z(t_f)} A_{s\,\text{n}}(z) \cdot dz . \qquad (8\text{--}4)$$

The potential, $\phi_{s\,\text{n}}(0)$, is the potential at the center of the feed point. The source electric field is limited to a gap region; if the gap is zero, the source is a delta function. The line integral of the vector potential runs from the center of the feed point to the point t_f on segment f in equation (8–4).

The $\text{EMF}_{s\,\text{n}}(t_{f\text{i}})$ in equation (8–4) is expanded with the Legendre polynomials to give the impedance matrix:

$$Z_{fs\,\text{mn}} = \sum_{i=0}^{M-1} \beta_{\text{mi}} \cdot \text{EMF}_{s\,\text{n}}(t_{f\text{i}}). \qquad (8\text{--}5)$$

The expansion matrix, β_{mi}, is computed with the Mth order Guassian integration formula, equation (7–7). The impedance matrix is computed by substituting equation (8–4) into equation (8–5). This computation of the impedance matrix naturally divides into two parts: the scalar and vector potential terms. Variables attributed to the scalar and vector potential terms in the impedance matrix are identified by the respective superscripts, s and v. The scalar and vector potentials can be expressed as a function of the potential integral, $\kappa_{s\,\text{n}}$, developed in section 6. A different notation is used for the potential integral, $\kappa_{s\,\text{n}}(t_{f\text{i}})$. The field point is indicated by the point $t_{f\text{i}}$ on the surface of segment f. The source is the nth basis function on segment s.

69

The scalar potential terms in $Z^S_{fs\ mn}$ divide into two cases: the triangular basis function, $\delta_{s\ 0}$, and the Legendre polynomial basis functions, $\eta_{s\ n}$. Each triangular current basis function contributes two square pulses to the scalar potential terms in submatrices $Z^S_{fs\ m0}$ in, equation (8–2). The general Legendre-polynomial charge basis functions are used to compute the scalar potential terms in the general term, $Z^S_{fs\ mn}$, in equation (8–2).

Each current basis function gives two square pulses for the charge distribution. The pulse on the source segment s has a height $-\delta_{s\ 0}/L$. The other pulse is on the previous segment, $s{-}1$, with a height $\delta_{s\ 0}/L$. Note, for the source triangular current basis function, $s = 1$, the $\kappa_{s-1\ 0}$ term is included in the image term:

$$Z^S_{fs\ m0} = -\sum_{i\,=\,0}^{M-1} \beta_{mi} \frac{1}{4\pi\epsilon_0}$$
$$\left[[\kappa_{s\ 0}(t_{fi}){-}\kappa_{s\ 0}(0))] \frac{-\delta_{s\ 0}}{L} + [\kappa_{(s-1)\ 0}(t_{fi}){-}\kappa_{(s-1)\ 0}(0)] \frac{\delta_{s\ 0}}{L} \right],$$

$$(8–6a)$$

for n = 0 and

$$Z^S_{fs\ mn} = -\sum_{i\,=\,0}^{M-1} \beta_{mi} \frac{1}{4\pi\epsilon_0} [\kappa_{s\ n}(t_{fi}){-}\kappa_{s\ n}(0)]\eta_{s\ n} \quad \text{for n > 0.} \qquad (8–6b)$$

The notation is simplified by introducing a new variable:

$$\Psi_{fs\ mn} = \sum_{i\,=\,0}^{M-1} \beta_{mi}\kappa_{s\ n}(t_{fi}). \qquad (8–7)$$

The constant, $\kappa_{s\ n}(0)$, gives only one expansion coefficient, $\Psi^C_{fs\ 0n}$. This constant is independent of the boundary-condition segment, f:

$$\Psi^C_{fs\ mn} = \delta_{m0}\kappa_{s\ n}(0).$$

The δ_{m0} is the usual Kronecker delta $\delta_{mm} = 1$ and $\delta_{mp} = 0$ for $p \neq m$. In this new notation, equation (8–6) reduces to

$$Z^S_{fs\,m0}P_m(t_f) = -\frac{1}{4\pi\epsilon_0}\left[\left[\Psi_{f(s-1)\,m0} - \Psi^C_{f(s-1)\,m0}\right]\frac{1}{L} - \left[\Psi_{fs\,m0} - \Psi^C_{fs\,m0}\right]\frac{1}{L}\right] \times$$

$$P_m(t_f)\delta_{s\,0} \quad \text{for n = 0,} \tag{8–8a}$$

$$Z^S_{fs\,mn}P_m(t_f) = -\frac{1}{4\pi\epsilon_0}\left[\Psi_{fs\,mn} - \Psi^C_{fs\,mn}\right]\eta_{s\,n}P_m(t_f) \quad \text{for n > 0.}$$

$$\tag{8–8b}$$

The factor, $P_m(t_f)$, is included in the equations (8–8) and (8–9) to emphasize that $Z^S_{fs\,mn}$ is the $P_m(t_f)$ expansion coefficient of the EMF on segment f. The notation can be simplified by replacing the quantity in the square bracket with a single variable, $T^S_{fs\,mn}$:

$$Z^S_{fs\,mn}P_m(t_f) = -\frac{1}{4\pi\epsilon_0}T^S_{fs\,mn}\chi_{s\,n}P_m(t_f). \tag{8–9}$$

The vector potential terms in the impedance matrix are computed by numerically integrating the vector potential. The numerical evaluations of integrals use polynomial approximations of the function. Therefore, it would be natural to expand the integrand in terms of Legendre polynomials. The Legendre polynomials can be integrated term by term to give Legendre polynomials. If both segments f and s are straight, then the final equation is a simple function of $\Psi_{fs\,mn}$.

The triangular current pulse is used to compute the first column of the impedance matrix. The higher order current basis functions are used to compute the remaining columns of the impedance matrix. The current pulse, δ_s (segment s and $s-1$), contribute the vector potential terms. Note, for the source triangular current basis function, $s = 1$, the $\kappa_{s-1\,0}$ and $\kappa_{s-1\,1}$ terms are included in the image term.

71

$$A_{s0}(t_{bi}) = \frac{-1}{4\pi c^2 \epsilon_0} \frac{1}{2} j\omega \left[[\kappa_{s\ 0}(t_{bi}) - \kappa_{s\ 1}(t_{bi})]\hat{u}_s + [\kappa_{s-1\ 0}(t_{bi}) + \kappa_{s-1\ 1}(t_{bi})]\hat{u}_{s-1} \right]\delta_s.$$

<div align="center">for n = 0.</div> (8–10a)

For the general case n > 0, the vector potential on segment b is given by a general expression,

$$A_{sn}(t_{bi}) = \frac{-1}{4\pi c^2 \epsilon_0} \frac{1}{2} j\omega \left[\frac{L}{2n+1}[\kappa_{s\ n+1}(t_{bi}) - \kappa_{s\ n-1}(t_{bi})]\hat{u}_s \right]\eta_{sn}.$$

(8–10b)

The line integral in equation (8–4) is evaluated by integrating each segment individually:

$$\int_0^{z(t_f)} A_{s\ n}(z)\cdot \mathrm{d}z = \sum_{b=1}^{f-1} \int_{\text{segment } b} A_{b\ n}(z)\cdot \mathrm{d}z + \int_{z(-1_f)}^{z(t_f)} A_{s\ n}(z)\cdot \mathrm{d}z.$$

(8–11)

The line integrals for segments 1 to segment f–1 are integrated over the entire segment. The last integral, the second term, is integrated over part of the segment.

The line integral element, dz, is converted to $\hat{u}_b$dz for each segment:

$$\int_0^{z(t_f)} A_{s\ n}(z)\cdot \mathrm{d}z = \sum_{b=1}^{f-1} \int_{\text{segment } b} A_{s\ n}(z)\cdot \hat{u}_b \mathrm{d}z + \int_{z(-1_f)}^{z(t_f)} A_{s\ n}(z)\cdot \hat{u}_f \mathrm{d}z.$$

(8–12)

In the general case, the integrand $A_{s\ n}(z)\cdot \hat{u}_b$ is expanding in terms of Legendre polynomials. The Legendre polynomials can be directly integrated by using equations (4–6) and (4–7).

If the unit vectors, $\hat{u}_b$, are constant on each segment, the A vector can be expanded with Legendre polynomials:

$$A_{s\,\mathrm{n}}(z(t_b)) = \frac{-1}{4\pi c^2 \epsilon_0} \frac{1}{2} j\omega \sum_{q=0}^{M} T^{\mathrm{V}}_{bs\,\mathrm{qn}} \mathrm{P}_q(t_b),\qquad (8\text{--}13)$$

where

$$\frac{-1}{4\pi c^2 \epsilon_0} \frac{1}{2} j\omega\, T^{\mathrm{V}}_{bs\,\mathrm{qn}} \mathrm{P}_q(t_b) = \sum_{i=0}^{M-1} \beta_{\mathrm{qi}} A_{sn}(z(t_{bi})).$$

If the vector, $\hat{u}_s$, implicit in the vector potential, $A_{s\,\mathrm{n}}(z)$, is a constant, then the expansion constant, $T^{\mathrm{V}}_{bs\,\mathrm{qn}}$, can be expressed in terms of $\Psi_{bs\,\mathrm{qn}}$:

$$T^{\mathrm{V}}_{bs\,\mathrm{q0}} \mathrm{P}_q(t_b) = \left[[\Psi_{bs\,\mathrm{q0}} - \Psi_{bs\,\mathrm{q1}}]\hat{u}_s + [\Psi_{b(s-1)\,\mathrm{q0}} + \Psi_{b(s-1)\,\mathrm{q1}}]\hat{u}_{s-1} \right] \mathrm{P}_q(t_b)$$

$$(8\text{--}14)$$

and

$$T^{\mathrm{V}}_{bs\,\mathrm{qn}} \mathrm{P}_q(t_b) = \frac{\mathrm{L}}{2n+1}\left[\Psi_{bs\,\mathrm{q(n+1)}} - \Psi_{bs\,\mathrm{q(n-1)}} \right]\hat{u}_s \mathrm{P}_q(t_b). \qquad (8\text{--}15)$$

The integral of the vector potential is simplified by substituting equation (8–13) into equation (8–12) and removing the constant factors from the integral. The dot product, $\hat{u}_b \cdot T^{\mathrm{V}}_{bs\,\mathrm{qn}}$, can be removed from the integral:

$$\int_{z(-1_b)}^{z(t_b)} A_{s\,\mathrm{n}}(z)\cdot\hat{u}_b \mathrm{d}z = \frac{-1}{4\pi c^2 \epsilon_0} \frac{1}{2} j\omega \sum_{q=0}^{M} \hat{u}_b \cdot T^{\mathrm{V}}_{bs\,\mathrm{qn}} \int_{z(-1_b)}^{z(t_b)} \mathrm{P}_q(2z/\mathrm{L})\mathrm{d}z. \qquad (8\text{--}16)$$

73

For a segment of length, L, the integration of $P_q(x_b)$ can be expressed as the product of a matrix, S_{qm}, and a column vector, $P_m(t_b)$:

$$\int_{z(-1_b)}^{z(t_b)} P_q(2z/L)dz = \sum_{m=0}^{\infty} \frac{L}{2} S_{qm} P_m(t_b),$$

(8–17)

where

$$S_{qm} = \frac{1}{2q+1}\left[\delta_m^{q+1} - \delta_m^{q-1}\right] \quad \text{For } q > 0$$

$$S_{0m} = \delta_0^m + \delta_1^m \qquad\qquad \text{For } q = 0.$$

The integral simplifies further if $t_b = 1$:

$$\int_{z(-1_b)}^{z(1_b)} P_q(2z/L)dz = L\delta_q^0.$$

(8–18)

The integral of the vector potential, $A_{s\,n}$, from the feed point to segment f is the sum of f terms:

$$\int_0^{z(t_f)} A_{s\,n}(z)\cdot dz = \frac{-1}{4\pi c^2 \epsilon_0}\frac{j\omega L}{4}\times$$
$$\left[\sum_{b=1}^{f-1} \hat{u}_b \cdot T^V_{bs\,0n} 2P_0(t_f) + \sum_{q=0}^{M} \hat{u}_f \cdot T^V_{fs\,qn}\sum_{m=0}^{\infty} S_{qm}P_m(t_f)\right].$$

(8–19)

The terms in the sum from $b = 1$ to $f - 1$ in equation (6–19) are constants; they contribute to the expansion coefficient of $P_0(t_f)$ of equation (8–19). The vector potential terms in the impedance matrix is

$$Z^V_{fs\,mn}P_m(t_f) = \frac{-1}{4\pi c^2 \epsilon_0}\frac{\omega^2 L}{4}\left[\sum_{b=1}^{f-1}\hat{u}_b \cdot T^V_{bs\,0n}2\delta^m_0 + \sum_{q=0}^{M}\hat{u}_f \cdot T^V_{fs\,qn}S_{qm}\right]P_m(t_f).$$

$$(8\text{--}20)$$

The terms in the sum from $b = 1$ to $f - 1$ in equations (6–20) and (6–21) only contribute to the $P_0(t_f)$ expansion term in the impedance matrix ($\delta^0_m = 0$ for $m \neq 0$).

The impedance matrix for a single basis function on one segment is

$$Z_{fs\,mn} = \frac{1}{4\pi\epsilon_0}\left[T^S_{fs\,mn} - \frac{\omega^2 L}{4c^2}\left[\sum_{b=1}^{f-1}\hat{u}_b \cdot T^V_{bs\,0n}2\delta^m_0 + \sum_{q=0}^{M}\hat{u}_f \cdot T^V_{fs\,qn}S_{qm}\right]\right],$$

$$(8\text{--}21)$$

where $n < N$ and $m < N$ for N basis functions and N_* boundary conditions per segment. The impedance matrix would include the contribution from all segments on both arms of the dipole. The symmetry in the dipole can be used to eliminate the coefficients of the image basis function as a variable, $\delta_{-s} = \delta_s$ and $\eta_{-s\,n} = -(-1)^n\eta_{s\,n}$ where $-s$ denotes the image. At the feed point, $s = 1$, the current pulse is split between the image and the antenna. At free-wire ends, the current pulse must vanish.

The basis functions and boundary condition discussed in this report allow a detailed analysis of the errors in the solution. The first step in this error analysis is to characterize the scalar potential terms in the impedance matrix. The magnitude of each term is determined by the expansion coefficients, $\Psi_{fs\,mn}$, for the potential integral, $\kappa_{s\,n}(t_f)$. First we will examine the static potential integral, $\kappa_{s\,n}(t_f)$, contribution to the magnitude of the

expansion coefficient, $\Psi_{fs\ mn}$. The plots in figures 6–2 and 6–3 show that the potential on the surface of the source segment has the same shape as the expansion functions, $P_m(t_s)$; consequently, the self-term, $\Psi_{ss\ nn}$, for the charge basis function, $P_n(t_s)$, will have the largest expansion coefficient. The other terms, $\Psi_{ss\ mn}$ $m = n\pm2$, $n\pm4$, etc., will be small for the self-term. The expansion coefficients, $\Psi_{ss\ mn} = 0$, are for the even and odd potentials when $m = n\pm1$, $n\pm3$, etc.

On the other hand, the *very sharp drop* in the static potential integral, $\kappa_n^s(t_{s\pm1})$, on the adjacent segment contributes to all of the expansion coefficients, $\Psi_{(s\pm1)s\ mn}$, for all m. The plots in figures 6–2b and 6–3b show that the scalar potentials and their expansion coefficients, $\Psi_{(s\pm d)s\ mn}$, are much smaller for $d \geq 2$. At large distances, the dipole potential, $\kappa_{s\ 1}(t_f)$, and the dipole potential created by each current basis function will be the dominate terms in the impedance matrix. The frequency-dependent part of the potential integral, $\kappa_n^f(t_f)$, is smooth function on all segments. The expansion coefficients of the frequency-dependent part of the potential integral term contributes terms, $\Psi_{fs\ mn}$, with $m = 0$, 1, and 2.

The computation of the boundary condition ignores expansion terms, $\Psi_{fs\ mn}$, with $m \geq N$. For the self-term, these terms will be small when the proper aspect ratio is used for each segment (table 7–1). Any errors introduced by neglecting these terms will be a high-order multipole moment. The high-order charge basis functions in the impedance matrix interact primarily with nearby segments.

The magnitude of the current terms depend on the constant, $\omega^2 L/4c^2$. An additional factor of L from the vector potential, from equation (8–15) ($n > 0$), can be included in this factor. The combined constant is $(\omega L/2c)^2$ for $n > 1$. In terms of the wavelength, λ, the constant reduces to $(\pi L/\lambda)^2$. The contribution of the high-order current basis functions to the impedance matrix can be made smaller by decreasing the segment size. For 10 segments per wavelength, this constant is $1/10$. For electrically small antennas, the cur-

rent term is a small correction to the static part of the impedance matrix. The high-order basis functions model the near fields as quasi-static interaction.

The magnitude of the current term is determined by the expansion coefficients, $\Psi_{fs\,mn}$, of the current basis functions. The expansion coefficients can be estimated from the current potential integral plotted in figures 6–4 and 6–5. The potential integral computed from the current basis functions does not have a sharp drop at the end of the source segment. In contrast to the charge basis function, the potential is small and smooth near the end of the segment. On the surface of nearby segments, the potential is a smooth function; it can be described with a few low-order Legendre polynomials, m = 0, 1, and 2. However, on the surface of the source segment, the current basis function, $J_{s\,n}$, gives two expansion coefficients, $\Psi_{ss\,n-1\,n-1}$ and $\Psi_{ss\,n+1\,n+1}$. *Note: the correct evaluation of the potentials on the adjacent segments requires both potential integrals, $\kappa_{s\,n-1}(t_s)$ and $\kappa_{s\,n+1}(t_s)$.* The integration of the two expansion coefficients give three terms: $\Psi_{ss\,n-2\,n-2}$, $\Psi_{ss\,nn}$, and $\Psi_{ss\,n+2\,n+2}$. The terms, $\Psi_{ss\,n-2\,n-2}$ and $\Psi_{ss\,n+2\,n+2}$, interact with charge basis functions, $P_{n-2}(t_s)$ and $P_{n+2}(t_s)$.

In the calculation of the impedance matrix, the high-order current term must be approximated. In a model with N basis functions per segment, the first N expansion coefficients, $\Psi_{ss\,00}$ to $\Psi_{ss\,N-1\,N-1}$, are included in the boundary condition. The expansion coefficients, $\Psi_{ss\,NN}$ to $\Psi_{ss\,N+1\,N+1}$, introduced by the current basis functions, $J_{s\,N-2}(t_s)$ and $J_{s\,N-1}(t_s)$, are not included in the impedance matrix. This approximation causes an P_N and P_{N+1} error in the EMF boundary condition. The boundary condition error can be calculated with the extra expansion coefficients, $\Psi_{fs\,mn}$, where $N \le m < M$. The solution is computed with the submatrix, $Z_{fs\,mn}$ (m < N). The submatrix, $Z_{fs\,mn}$ ($N \le m < M$), is used to compute the error α_{fm} from the solution. The magnitude of the off-diagonal elements in the impedance matrix depends on the constant, $(\pi L/2\lambda)^2$.

In principle, the order of the terms in the impedance matrix, equation (8–2), does not affect the accuracy of the solution. In practice, the numerical roundoff errors in the

solution process can create large errors in the numerical solution (Press et al., 1986). The numerical accuracy of the solution can be improved using partial or full pivoting. Pivoting moves the large elements to the diagonal of the matrix. Thus, the large self-interaction terms, $Z_{ss\ pp}$, in the impedance matrix should be moved to the diagonal. However, the self-interaction terms, $Z_{ss\ pk}$, with $p \neq k$ are small; these terms should be off the matrix diagonal. Equation (8–2) has the large submatrices, $Z_{fs\ pp}$, on the diagonal. In complex problems, the large submatrices, $Z_{fs\ pp}$, may require additional pivoting. For a dipole, the large elements are already on the diagonal of the submatrix, $Z_{fs\ pp}$. Gaussian elimination is used on the small upper triangular part of the matrix. Back substituting is used to compute the final solution.

Figures 8–1 and 8–2 show the logarithm of the magnitudes of the impedance matrix elements for a dipole at resonances. The dipole parameters are the total length, $2h = 1$m; the wire radius, $a = 4.5401$E–5; and input frequency, 146.0 MHz. The colors, red, purple, blue, green, yellow, and red indicate a range of values from 1 to 1E–6. Matrix elements smaller than 1E–6 are plotted as black. Figure 8–1 shows a 56-segment model with one basis function per segment; the impedance matrix is the submatrix, $Z_{fs\ 00}$. Figure 8–2 shows an 8-segment model with seven basis functions per segment. In figure 8–2, 45.7% of the matrix elements are black. In Figure 8–2, the diagonal elements, $Z_{ss\ nn}$, in the matrix are self-interaction terms for each basis function on each segment, the $\Psi_{ss\ nn}$ expansion terms. The peaks parallel to the diagonal, $Z_{ss\ n(n\pm2)}$ are the current interaction terms, $\Psi_{ss\ (n\pm2)n}$; and the self-interaction terms, $\Psi_{ss\ mn}$. The other terms in the peaks, $Z_{s(s\pm1)\ nm}$, are the nearest neighbor interactions, $\Psi_{s(s\pm1)\ nm}$. The peaks in the impedance matrix model the near field. The elements between the peaks model the far field. The far field is modeled by the P_0 and P_1 basis functions. The structure of the impedance matrix, in figure 8–2, should improve the accuracy of the solution to the impedance matrix.

LEFTMOUSE ROTATES: (900, -5, 330, 0.00, 0.00, 0.00)
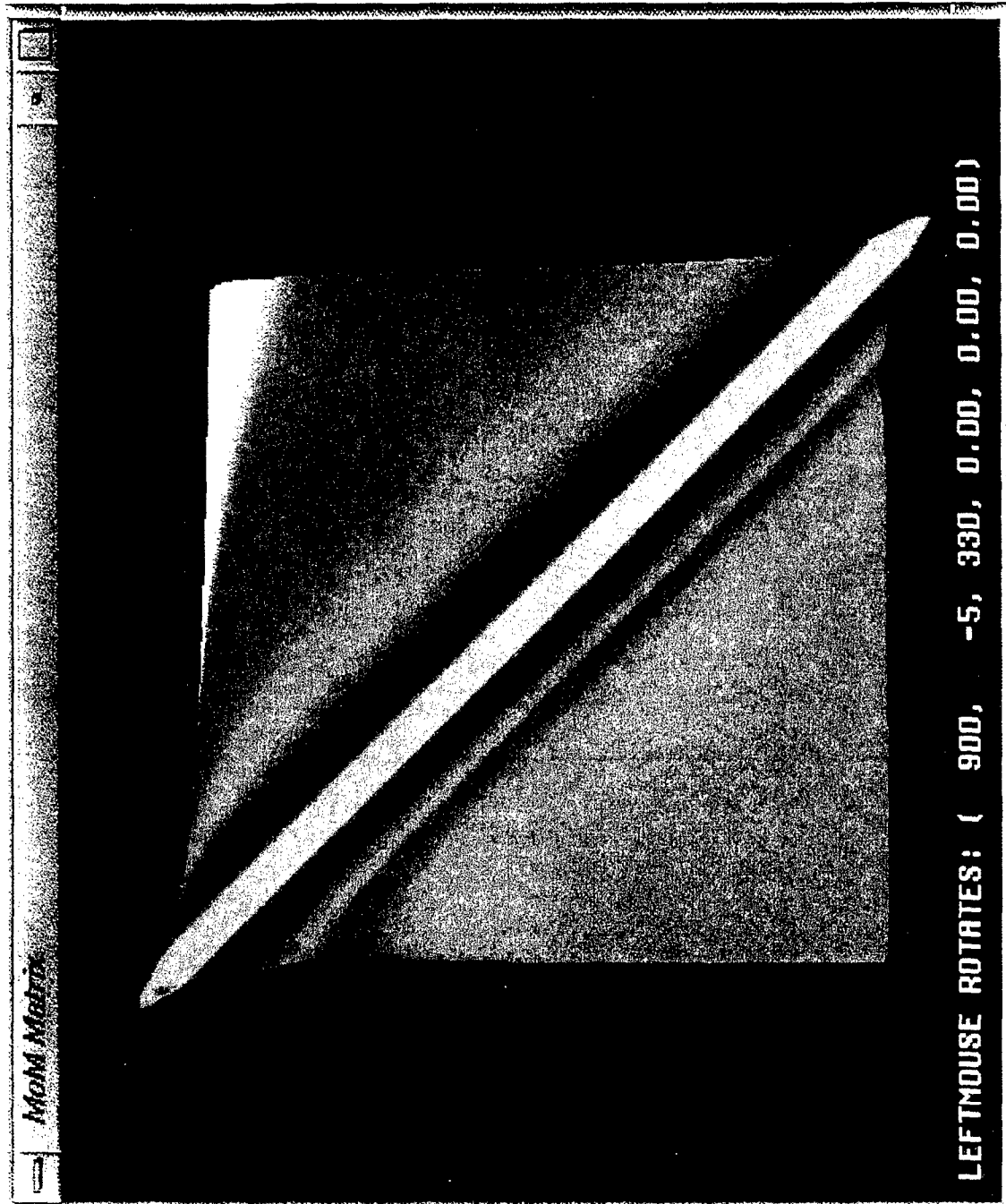
Figure 8-1. A logarithmic plot of the magnitude of the elements in the impedance matrix for a 56-segment model with one basis function per segment. The antenna parameters in figure 2-4 are used in this calculation.
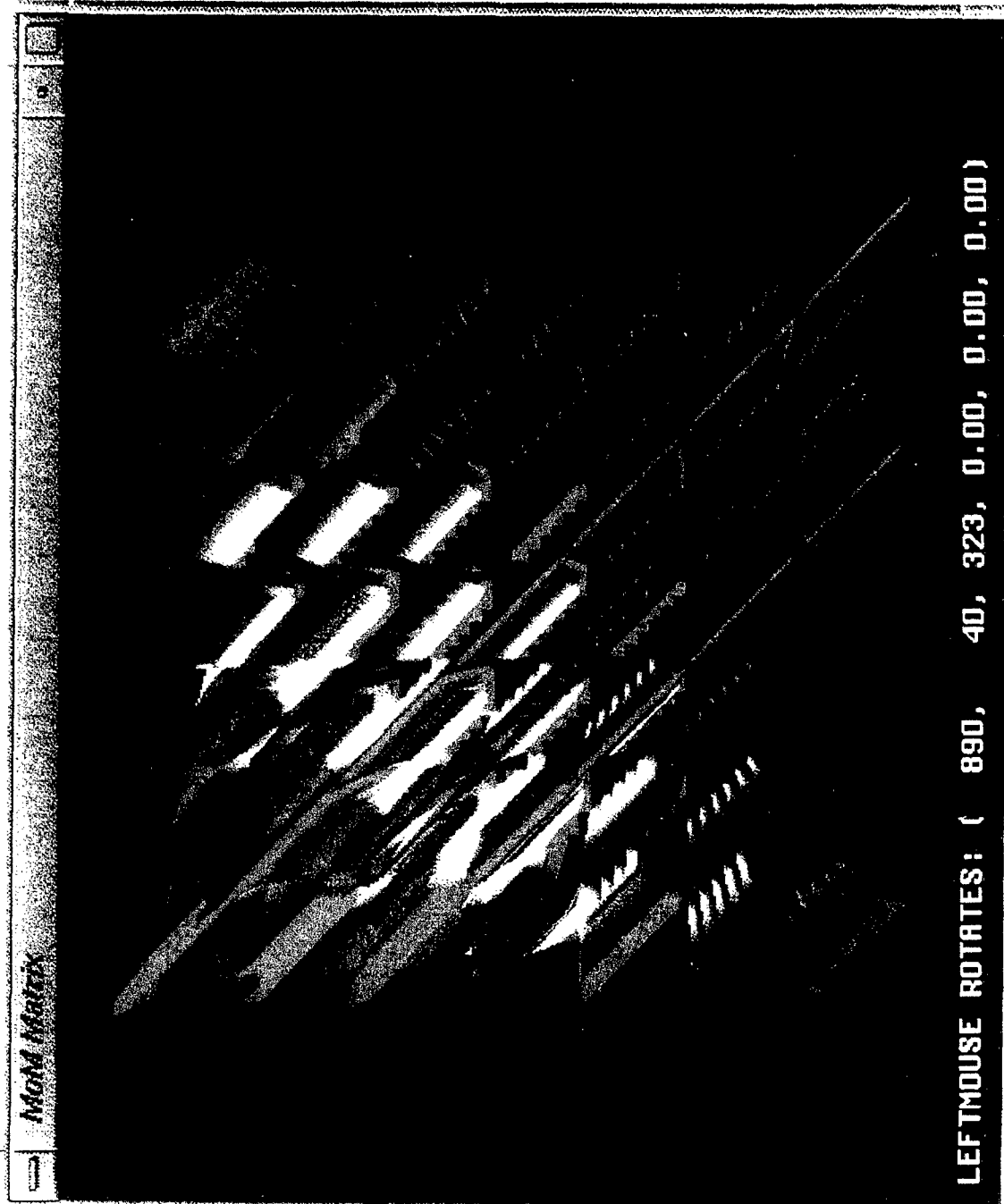
Figure 8-2. A logarithmic plot of the magnitude of the elements in the impedance matrix for a 8-segment model with seven basis function per segment. The antenna parameters in figure 2-4 are used in this calculation.

Insight into these errors can be gained by using Singular Value Decomposition (Press et al., 1986). A matrix problem can be solved by using the eigenvectors and eigenvalues of the matrix. The ith eigenvalues, λ_i, and eigenvectors, x_i, obey equation (8–22):

$$\lambda_i x_i = A x_i. \tag{8–22}$$

In this discussion, we will assume that $\lambda_i \neq 0$. The solution, S, to the matrix problem,

$$Y = AS, \tag{8–23}$$

can be found by expanding column vector, Y, in a sum of eigenvectors

$$Y = \sum_{i=0}^{N-1} s_i x_i, \tag{8–24}$$

where

$$s_i = Y \cdot x_i. \tag{8–25}$$

The solution is

$$S = \sum_{i=0}^{N-1} \frac{s_i}{\lambda_i} x_i. \tag{8–26}$$

The equation allows the effects of roundoff errors to be estimated. The calculation of the expansion coefficient, s_i, will include roundoff error. This error is weighted by the $1/\lambda_i$. A small eigenvector will cause a large error in the solution, S. The numerical stability of a matrix, the condition number, is measured by the ratio of the largest and smallest eigenvalue. The condition number is always larger than one:

$$C = \left| \frac{\lambda_{max}}{\lambda_{min}} \right|. \qquad\qquad (8\text{--}27)$$

A high-condition number matrix can have large numerical errors.

The condition number is used to compare the numerical stability of the impedance matrices plotted in figures 8–1 and 8–2. The condition numbers for figures 8–1 and 8–2 are 397.00 and 89.96, respectively. A single-precision impedance matrix is used to compute the condition number. The high-order basis functions and boundary condition simplifies the impedance matrix and reduce the condition number.

In general, one would expect the condition number to be a function of both the number of segments and the number of basis functions per segment. Table 8–1 shows the condition number as a function of the number segments (6, 12, and 24) and of the number of basis functions per segment (1 to 7). The existing program is limited to 97 unknowns.

Table 8–1. Condition number of dipole at resonance.

Number of Basis Functions	6 Segs.	12 Segs.	24 Segs.
1	69.51	120.90	208.23
2	68.36	119.69	206.3
3	70.06	123.77	215.66
4	70.14	123.95	
5	70.50	124.79	
6	70.59	124.99	
7	70.76	125.37	

Table 8–1 shows that the condition number is independent of the number of basis functions used on each segment. The condition number depends only on the submatrix, $Z_{fs\,00}$. The high-order basis functions can be added to model the fine details in the charge distribution *without increasing the condition number.*

The condition number for a dipole at antiresonance is much smaller. The condition number at antiresonance is calculated for a 12-segment model. Table 8–2 shows seven different models.

Table 8–2. Condition number of a dipole at antiresonance.

Number of Basis Functions	12 Segs.
1	6.3002
2	6.273
3	6.4906
4	6.5077
5	6.5566
6	6.5728
7	6.5965

The impedance matrix is stable at antiresonance. The current and charge distribution should be accurate on the antenna. However, at the feed point, the current will be very small. A small numerical error in the overall solution would have a larger impact at the feed point.[6] The numerical results in section 2 show that this is not a problem with our algorithm.

---

6. D. Fern, personal communication

The Legendre-polynomial basis functions are closely related to the power series basis functions used by Djordjevic et al. (1990). The two sets of basis functions, in principle, are equivalent; however, the numerical structure of the impedance matrices has important differences. Each power series basis function has a $1/|r-r'|$ term in its potential integral. The net charge on the segment determines the magnitude of the $1/|r-r'|$ term. For a basis function t^m ($0 \leq t \leq 1$), the net charge is $1/(m+1)$. The details modeled by the high-order power series basis functions are lost in the numerical noise at large distances. The Legendre-polynomial basis function, P_n, replaces the $1/|r-r'|$ term with a much smaller $1/|r-r'|^{n+1}$ term. Each Legendre-polynomial basis function represents a distinguishable part of the near fields. The condition number is independent of the number of Legendre polynomial basis functions used on each segment.

The equal-width, square-pulse testing boundary condition used by Djordjevic et al. (1990) can be compared to the EMF boundary condition by using a matrix transformation of the impedance matrix, equation (8–1). The calculation of this matrix transformation uses two steps. The impedance matrix is used to estimate the EMF on each segment. The $EMF(t)_{est}$ on segment f is

$$EMF(t_f)_{est} = \sum_{m=0}^{M} \sum_{n=0}^{N-1} \sum_{s=1}^{R} Z_{fs\,mn} P_m(t_f) \chi_{sn},$$
(8–28)

where M is the number of Gaussian quadrature points used to calculate the impedance matrix. The high-order error estimation terms, $M > N$, improve the accuracy of the EMF estimate.

The equal-width, square-pulse testing boundary condition can be evaluated from the $EMF(t_f)_{est}$:

$$\int_{z(t_i)}^{z(t_{i+1})} E(z) \cdot dz = \text{EMF}(t_{fi+1})_{est} - \text{EMF}(t_{fi})_{est} , \tag{8-29}$$

where t_i and t_{i+1} are the end points of the pulse testing function. The square-pulse testing boundary condition, $\text{BC}^{pt}_{f\,i}$, for the ith pulse on the segment f is

$$\text{BC}^{pt}_{f\,i} = \sum_{m=0}^{M} \sum_{n=0}^{N-1} \sum_{s=1}^{R} Z_{fs\,mn} [P_m(t_{fi+1}) - P_m(t_{fi})] \chi_{sn} . \tag{8-30}$$

The new impedance matrix for the point match boundary condition is the coefficient of χ_{sn}

$$Z^{pt}_{fs\,in} = \sum_{m=0}^{M} Z_{fs\,mn} [P_m(t_{fi+1}) - P_m(t_{fi})] . \tag{8-31}$$

This transformation is the sum of the rows of the matrix where the quantity in the square bracket is the weighting coefficient for each row. The effect of the transformation is to add the large diagonal term, $Z_{ss\,nn}$, to the small off-diagonal terms in the matrix. The addition of the large term causes additional roundoff in the matrix element. To solve the matrix, this transformation is reversed; rows are subtracted to eliminate off-diagonal elements in the matrix. The combined effect of the transformation and solution of the matrix is an increase in roundoff error in the solution of the impedance matrix.

The equal-width, square-pulse testing boundary condition will not work for high-order Legendre-polynomial basis functions. The equal-width, square-pulse testing functions are wider than the oscillation of $\kappa_{s\,n}(t_s)$ near the end of the segment. The EMF boundary condition can resolved the fine details modeled by the high-order Legendre-polynomial basis functions. The EMF boundary condition isolates the interaction of the basis functions on

85

different segments. The stability of this impedance matrix is illustrated in the condition number calculations and numerical calculations.

9 CONCLUSIONS

The error in the method of moments depends on the models used to approximate the charge distribution and the boundary condition. The modeling errors in the charge distribution and the boundary condition interact through the scalar and vector potentials. The basis functions and the boundary condition are selected to minimize the interaction of the two modeling errors. The algorithm used to impose the boundary condition also estimates the error in the boundary condition.

The basis functions model the charge distribution on each segment with a multipole expansion of the charge distribution. The first basis function models the net charge on each segment. The higher order basis functions are used to redistribute the charge to eliminate the parallel component of the electric field on the segment. The higher order basis functions model the detail in the near field of the segment. The far fields of the higher order basis functions are small. The charge distribution on one segment primarily interacts with the nearby segments.

The modeling errors in the boundary condition implies an error in the charge distribution. The charge distribution error caused by the boundary condition is a high-order multipole moment. The boundary condition modeling error on different segments are isolated from each other. The basis functions and boundary condition modeling errors are local to each segment. This creates a more stable impedance matrix. The condition number of the impedance matrix is independent of the number of basis functions per segment. The condition number depends only on the number of segments in the model.

The computed charge distribution agrees with the theoretical calculations of the charge distribution. The high-order basis functions give the best model of the charge distribution near the end of the wire. The charge distribution converges much quicker for the high-order basis functions. For small matrix models, the high-order basis functions are more accurate.

For large matrix models, the convergence of the admittance depends on the matrix size used to model the dipole. The current at the feed point of the dipole depends only on the height of the triangular current basis function. The height is computed very accurately by the boundary condition algorithm. Even the square and linear charge basis function models are accurate at resonance and antiresonance. This shows that the error in the boundary condition is a high-order multipole moment.

The numerical examples discussed in this report have high aspect-ratio segments. For lower aspect-ratio segments, the shape of the potentials near the end of the segment impacts the evaluation of the boundary condition. Additional work needs to be performed to understand the limitation introduced by lower aspect-ratio segments. The current work could be extended to model general symmetric dipoles without loops.

The basis functions and boundary condition simplify the structure of the impedance matrix. The far field interaction is modeled by the triangular current basis functions. The near field is modeled by the high-order basis functions. This approach combines the flexibility of the full-wave approach with the stability of the quasi-static approach. The algorithm is accurate for both the near and far fields of the antenna. The error estimation should be a useful tool in evaluating the errors in the electric-field boundary condition.

10 REFERENCES

Butler, C. M. 1975. "Evaluation of Potential Integral at Singularity of Exact Kernel in Thin-Wire Calculations," *IEEE Transactions on Antennas and Propagation,* AP–23(Mar), pp. 293–295.

Canning, F. 1992. "Sparse Approximation for Solving Integral Equations with Oscillatory Kernels," *Siam Journal Scientific and Statistical Computing,* vol. 13, no. 1(Jan), pp. 71–87.

Djordjevic, A. R., M. B. Bazdar, G. M. Vitosevic, T. K. Sarkar, and R.F. Harrington. 1990. *Analysis of Wire Antennas and Scatterers: Software and User's Manual.* Artech House, Boston, MA.

Dudley, D. G. 1995. "Error Minimization and Convergence in Numerical Methods," *Electromagnetic,* vol. 5, pp. 89–97.

Feynman, R. P., R. B. Leighton, and M. Sands. 1964. *The Feynman Lectures on Physics, Volume II.* pp. 18–10, Addison-Wesley Publishing Co., Reading, MA.

Gradshteyn, I. S. and I. M. Ryzhik. 1980. *Table of Integrals, Series, and Products. Corrected and Enlarged Edition.* Academic Press, Inc. Orlando, FL.

Harrington, R. F. 1968. *Field Computation by Method of Moments.* Macmillan Company, New York.

Hwu, S. U. and D. R. Wilton. 1988. "Electromagnetic Scattering and Radiation by Arbitrary Configurations of Conducting Bodies and Wires," NOSC TD 1325 (Aug), Naval Command, Control and Ocean Surveillance Center RDT&E Division,[*] San Diego, CA.

Jackson, J. D. 1975. *Classical Electrodynamics*, John Wiley & Sons, Inc., New York, NY.

King, R. W. P. 1956. *The Theory of Linear Antennas; with Charts and Tables for Practical Applications*, Harvard University Press, Cambridge, MA.

Logan, J. C. and J. W. Rockway. 1986. "The New MININEC (Version 3): A Mini-Numerical Electromagnetic Code," NOSC TD 938 (Sep), Naval Command, Control and Ocean Surveillance Center RDT&E Division,[*] San Diego, CA.

Michalski, K. A. and C. M. Butler. 1983. "An Efficient Technique for Solving the Wire Integral Equation with Non-uniform Sampling," *IEEE Southeastcon Conference Proceedings* (April).

Popovic, B. D., M.B. Dragovic, and A. R. Djordjevic. 1982. *Analysis and Synthesis of Wire Antennas.* Research Studies Press, New York, NY.

Press, W. H., B. P. Flannery, S. A. Teukolsky, and W. T. Vetterling. 1986. *Numerical Recipes the Art of Scientific Computing.* Cambridge University Press, Cambridge, United Kingdom.

* Formerly Naval Ocean Systems Center (NOSC).

Richmond, J. H. 1965 "Digital Computer Solutions of the Rigorous Equations for Scattering Problems," *Proceedings of the IEEE* (pp. 796–805). August.

Watt, A. D. 1967. *VLF Radio Engineering.* pp. 403, Pergamon Press, New York, NY.

APPENDIX A: NUMERICAL CALCULATION OF POTENTIAL INTEGRAL

In equation (6–2), the z' integration can be simplified by integrating the potential integral by parts n times in z' and using equation (4–8). As a simple example, consider $\kappa_1^S(\rho,z)$:

$$\kappa_1^S(\rho,z) = \frac{1}{2\pi}\int_0^{2\pi}\int_{-L/2}^{L/2} P_1(2z'/L)\frac{1}{|r-r'|}\,dz'\,d\varphi', \qquad (A-1)$$

where $|r-r'| = [(z-z')^2+\rho^2+a^2-2a\rho\cos\varphi']^{1/2}$. Integrating by parts:

$$\kappa_1^S(\rho,z) = \frac{1}{2\pi}\int_0^{2\pi}\left[\frac{(z'^2-(L/2)^2)}{L}\frac{1}{|r-r'|}\Bigg|_{-L/2}^{L/2} - \int_{-L/2}^{L/2}\frac{(z'^2-(L/2)^2)d}{L}\frac{1}{dz'|r-r'|}\,dz'\right]d\varphi'.$$

$$(A-2)$$

The first term is zero at $\pm L/2$:

$$\kappa_1^S(\rho,z) = -\frac{1}{2\pi}\int_0^{2\pi}\int_{-L/2}^{L/2}\frac{(z'^2-(L/2)^2)}{L}\frac{d}{dz'}\frac{1}{|r-r'|}dz'\,d\varphi'. \qquad (A-3)$$

The derivative simplifies to

$$\frac{d}{dz'}\frac{1}{|r-r'|} = \frac{(z-z')}{|r-r'|^3}, \qquad (A-4)$$

$$\frac{d}{dz'}\frac{1}{|r-r'|} = P_1(\cos\theta)\frac{1}{|r-r'|^2}, \qquad (A-5)$$

where $\cos\theta = \dfrac{z-z'}{|r-r'|}$. The angle θ is measured from the z-axis.

$$\kappa_1^s(\rho,z) = -\frac{1}{2\pi} \int_0^{2\pi} \int_{-L/2}^{L/2} \frac{(z'^2 - (L/2)^2)}{L} \frac{P_1(\cos\theta)}{|\,r-r'\,|^2} \, dz' \, d\varphi'. \tag{A-6}$$

At large distance, $|\,r\,| \gg L/2$, θ and $|\,r-r'\,|$ are almost constant. The integral can be approximated as

$$\kappa_1^s(\rho,z) = \frac{P_1(\cos\theta)}{|\,r\,|^2} \int_{-L/2}^{L/2} \frac{((L/2)^2 - z'^2)}{L} dz', \tag{A-7}$$

$$\kappa_1^s(\rho,z) = Q \frac{L}{8} \frac{P_1(\cos\theta)}{|\,r\,|^2} \int_{-1}^{1} (1-t^2) dt, \tag{A-8}$$

$$\kappa_1^s(\rho,z) = Q \frac{L}{6} \frac{P_1(\cos\theta)}{|\,r\,|^2} \quad \text{for } |\mathrm{r}| \gg L/2. \tag{A-9}$$

This integral is the dipole potential at large distances.

In the general case,

$$\kappa_n^s(\rho,z) = \frac{1}{2\pi}(-1)^n \int_0^{2\pi} \int_{-1}^{1} \left[\frac{(z'^2 - 1)^n}{2^n n!} \right] \frac{d^n}{dz'^n} \frac{1}{|\,r-r'\,|} \, dz' \, d\varphi'. \tag{A-10}$$

The derivative of the static potential integral can be reduced to

$$\frac{d^n}{dz'^n} \frac{1}{|\,r-r'\,|} = n! P_n(\cos(\theta))/|\,r-r'\,|^{-n-1}. \tag{A-11}$$

The final integral is

$$\kappa_n^S(\rho,z) = \frac{1}{2\pi}\int_0^{2\pi}\int_{-1}^{1}\left[\frac{(1-z'^2)^n}{2^n}\right]\frac{P_n(\cos(\theta))}{|r-r'|^{n+1}}\,dz'\,d\varphi'. \tag{A-12}$$

The far-field form of the potential integral is explicit in equation (A–12). At large distances, the integrand is a slowly varying function; the numerical integration is very accurate. Equation (A–12) is also used to calculate the potential integral close to the wire.

In the near field, the equation (6–2) must be directly evaluated. In this case, the term $\ln((1+\tau)/(1-\tau))$ is not accurate for τ near 1. Several alternate forms exist for $\ln((1+\tau)/(1-\tau))$ for $\tau > .5$:

$$\kappa_0^S(\rho,z) = \frac{Q}{LN}\sum_{i=0}^{N-1}\ln\left[\frac{R_1+z+L/2}{R_2+z-L/2}\right] \quad \text{for } z > L/2, \tag{A-13}$$

$$\kappa_0^S(\rho,z) = \frac{Q}{LN}\sum_{i=0}^{N-1}\ln\left[\frac{R_2-z+L/2}{R_1-z-L/2}\right] \quad \text{for } z < -L/2, \tag{A-14}$$

and

$$\kappa_0^S(\rho,z) = \frac{Q}{LN}\sum_{i=0}^{N-1}\ln\left[\frac{(z+L/2+R_1)(R_2-z+L/2)}{\rho^2+a^2-2a\rho x_i}\right] \quad \text{for } |z| < L/2, \tag{A-15}$$

where

$$R_1 = \sqrt{\rho^2+a^2+(z+L/2)^2-2a\rho x_i} \quad \text{and} \quad R_2 = \sqrt{\rho^2+a^2+(z-L/2)^2-2a\rho x_i}.$$

Equation (A—15) can be simplified by separating the numerator and denominator:

$$\kappa_0^S(\rho,z) = \frac{Q}{LN} \sum_{i=0}^{N-1} \ln[(z+L/2+R_1)(R_2-z+L/2)] - \ln(\rho^2+a^2-2a\rho x_i)]$$

$$\text{for } |z| < L/2. \tag{A—16}$$

The first term is almost constant; the numerical evaluation converges very quickly. The second term can be analytically evaluated:

$$\frac{2\pi}{N} \sum_{i=0}^{N-1} \text{Ln}[\rho^2+a^2-2a\rho x_i] = \int_0^{2\pi} \ln[\rho^2+a^2-2a\rho\cos(\varphi)]d\varphi. \tag{A—17}$$

The integral is the potential integral of an infinite cylinder of radius a. This integral can be evaluated with

$$\int_0^{2\pi} \ln[c+d\cos(\varphi)]d\varphi = 2\pi\ln\left[\frac{c+\sqrt{c^2-d^2}}{2}\right] \text{ for } c \geq |d| > 0, \tag{A—18}$$

where $c = \rho^2+a^2$ and $d = 2a\rho$. The square root term simplifies to $\sqrt{c^2-d^2} = \sqrt{(\rho^2-a^2)^2}$. The square root is ρ^2-a^2 for $\rho \geq a$ and $a^2-\rho^2$ for $\rho \leq a$:

$$\int_0^{2\pi} \ln[\rho^2+a^2-2a\rho\cos(\varphi)]d\varphi = 2\pi\ln(\rho^2) \quad \text{for } \rho \geq a, \tag{A—19a}$$

and

$$\int_0^{2\pi} \ln[\rho^2+a^2-2a\rho\cos(\varphi)]d\varphi = 2\pi\ln(a^2) \quad \text{for } \rho < a. \tag{A—19b}$$

This is the expected result for an infinite cylinder. The term, $Ln[\rho^2+a^2-2a\rho x_i]$, in equation (A–16) can be replaced by $Ln[\rho^2]$ for $\rho \geq a$ or $Ln[a^2]$ for $\rho < a$. Equation (A–15) reduces to

$$\kappa_0^S(\rho,z) = \frac{Q}{LN} \sum_{i=0}^{N-1} \ln\left[\frac{(z+L/2+R_1)(R_2-z+L/2)}{\rho^2}\right]$$

for $|z| < L/2$ and $\rho \geq a$, $\qquad$ (A–20a)

$$\kappa_0^S(\rho,z) = \frac{Q}{LN} \sum_{i=0}^{N-1} \ln\left[\frac{(z+L/2+R_1)(R_2-z+L/2)}{a^2}\right]$$

for $|z| < L/2$ and $\rho < a$. $\qquad$ (A–20b)

Equations (A–20a) and (A–20b) are valid for $|z| < L/2$; however, when $|z| = L/2$ and $\rho = a$, the numerator vanishes. In this case, equations (A–13) and (A–14) are used to compute the potential. For $z = L/2$, the term, R_2, reduces to $\sqrt{\rho^2+a^2-2a\rho x_i}$. For $z = -L/2$, the term, R_1, reduces to $\sqrt{\rho^2+a^2-2a\rho x_i}$:

$$\kappa_0^S(\rho,z) = \frac{Q}{LN} \sum_{i=0}^{N-1} \ln\left[\frac{R_1+L}{\sqrt{\rho^2+a^2-2a\rho x_i}}\right] \quad \text{for } z = L/2, \qquad \text{(A–21a)}$$

$$\kappa_0^S(\rho,z) = \frac{Q}{LN} \sum_{i=0}^{N-1} \ln\left[\frac{R_2+L}{\sqrt{\rho^2+a^2-2a\rho x_i}}\right] \quad \text{for } z < -L/2. \qquad \text{(A–21b)}$$

The procedure used to simplify equations (A–20) gives

$$\kappa_0^S(\rho,z) = \frac{Q}{LN} \sum_{i=0}^{N-1} \ln\left[\frac{R_1+L}{a}\right] \quad \text{for } z = L/2 \text{ and } \rho \leq a \qquad \text{(A–22a)}$$

and

$$\kappa_0^s(\rho,z) = \frac{Q}{LN} \sum_{i=0}^{N-1} \ln\left[\frac{R_2+L}{a}\right] \quad \text{for } z = -L/2 \text{ and } \rho \le a. \tag{A-22b}$$

For the case, $\rho > a$,

$$\kappa_0^s(\rho,z) = \frac{Q}{LN} \sum_{i=0}^{N-1} \ln\left[\frac{R_1+L}{\rho}\right] \quad \text{for } z = L/2 \text{ and } \rho > a \tag{A-22c}$$

and

$$\kappa_0^s(\rho,z) = \frac{Q}{LN} \sum_{i=0}^{N-1} \ln\left[\frac{R_2+L}{\rho}\right] \quad \text{for } z = -L/2 \text{ and } \rho > a. \tag{A-22d}$$

Equations (A–13), (A–14), (A–20), (A–21), and (A–22) give the best convergence and accuracy in the region close to the wire.

In the near field, the potential integral can be computed in closed form. The exact calculation involves large cancellations at moderate distances from the wire. Only minor simplifications are possible.

$$\kappa_1^s(\rho,z) = \frac{Q}{LN} \sum_{i=0}^{N} \frac{2z}{L}\left(\ln\left[\frac{1+\tau}{1-\tau}\right] - 2\tau\right), \tag{A-23}$$

$$\kappa_2^s(\rho,z) = \frac{Q}{LN} \sum_{i=0}^{N} \frac{3}{2}\left[\frac{R_1+R_2}{L} - \frac{12z^2}{L^2}\tau + \left(4\frac{z^2}{L^2} - 2\alpha^2\right)\ln\left[\frac{1+\tau}{1-\tau}\right]\right] - \frac{1}{2}\ln\left[\frac{1+\tau}{1-\tau}\right], \tag{A-24}$$

$$\kappa_3^s(\rho,z) = \frac{Q}{LN} \sum_{i=0}^{N} \frac{12}{L^3}\left[\frac{5}{12}Lz(R_1+R_2) - 2z\tau\left[\frac{11}{6}z^2 + \frac{L^2}{12} - \frac{2}{3}\alpha^2\right] + z(z^2 - \frac{3}{2}\alpha^2)\ln\left[\frac{1+\tau}{1-\tau}\right]\right]$$

$$- \frac{3}{2}\Psi_1(\rho,z), \tag{A-25}$$

INITIAL DISTRIBUTION

Code D0012	Patent Counsel	(1)
Code D0271	Archive/Stock	(6)
Code D0274	Library	(2)
Code D0271	Dave Richter	(1)
Code D14	Larry D. Flesner	(1)
Code D364	Everett W. Jacobs	(1)
Code D83	Dennis M. Bauman	(1)
Code D835	Gary J. Brown	(1)
Code D8505	John W. Rockway	(1)
Code D8505	James R. Zeidler	(1)
Code D851	Lance B. Koyama	(1)
Code D851	Shing T. Li	(1)
Code D851	James C. Logan	(1)
Code D851	Linda C. Russell	(1)

Defense Technical Information Center
Fort Belvoir, VA 22060–6218 (4)

NCCOSC Washington Liaison Officer
Washington, DC 20363–5100

Center for Naval Analyses
Alexandria, VA 22302–0268

Navy Acquisition, Research and Development
    Information Center (NARDIC)
Arlington, VA 22244–5114

GIDEP Operations Center
Corona, CA 91718–8000

Office of Naval Research
800 N. Quincy Street
Att. 311, Dr. Richard L. Lau
Arlington, VA 22217–5660

Office of Naval Research
800 N. Quincy Street
Att. 313, Dr. William Stachnik
Arlington, VA 22217–5660

Headquarters US Army
    Communications–Electronics Command
AMSEL–RD–ST–C
(Dr. Felix Schwering)
Fort Monmouth, NJ 07703–5000

Rockwell International Science Center, Inc.
Dr. Francis X. Canning
1049 Camino Dos Rios
Thousand Oaks, CA 91360

Lawrence Livermore National Laboratory
Gerald J. Burke
L–156
P.O. Box 5504
Livermore, CA 94550

Clemson University
Dr. Chalmers M. Butler
Department Electrical and Computer Engineering
Clemson, SC 29634–0915

Syracuse University
Dr. Roger F. Harrington
Department Electrical and Computer Engineering
121 Link Hall
Syracuse, NY 13244–1240

University of Illinois
Dr. Raj Mittra
Department Electrical and Computer Engineering
1406 West Green Street
Urbana, IL 61801

University of Houston
Dr. Donald R. Wilton
Department Electrical and Computer Engineering
Houston, TX 77204–4793

Replacement page